

---

This manuscript is a preprint and has yet to undergo peer-review. Please note that subsequent versions of this manuscript may have different content. If accepted, the final version of this manuscript will be available via the 'Peer-reviewed Publication DOI' link on the right-hand side of this webpage. Please feel free to contact any of the authors; we welcome feedback.

---

1 **Lateral variability in strain along a mass-transport complex (MTC) toewall:**  
2 **a case study from the Makassar Strait, offshore Indonesia**

3 Harya D. Nugraha<sup>1,2\*</sup>, Christopher A-L. Jackson<sup>1</sup>, Howard D. Johnson<sup>1</sup>, and David M. Hodgson<sup>3</sup>

4 <sup>1</sup>*Basins Research Group (BRG), Department of Earth Science and Engineering, Imperial College,*  
5 *London SW7 2BP, UK*

6 <sup>2</sup>*Department of Geological Engineering, Universitas Pertamina, Jakarta 12220, Indonesia*

7 <sup>3</sup>*Stratigraphy Group, School of Earth and Environment, University of Leeds, Leeds LS2 9JT, UK*

8 *\*Corresponding author (email: [harya.nugraha14@imperial.ac.uk](mailto:harya.nugraha14@imperial.ac.uk))*

9 **Abstract:** Contractional features characterise the toe domain of mass-transport complexes (MTCs).  
10 Their frontal geometry is typically classified as frontally-confined or frontally-emergent. However, it  
11 remains unclear how frontal emplacement style and contractional strain within an MTC can vary along  
12 strike. We use bathymetry and 3D seismic reflection data to investigate lateral variability of frontal  
13 emplacement and strain within the toe domain of a recent MTC (the Haya Slide) in the Makassar Strait.  
14 The slide originated from an anticline flank collapse, and the toe domain is characterised by a radial  
15 fold-and-thrust belt that reflects southwestwards emplacement. The degree of frontal confinement  
16 and overall toe domain structural style changes laterally, from frontally-confined in the S (associated  
17 with a deeply-incised, c. 200 mbsf, planar basal shear surface), to frontally-emergent in the W  
18 (associated with a shallowly incised, c. 120 mbsf, NE-dipping, c. 3°, basal shear surface). Quantitative  
19 strain analysis shows c. 8-14% shortening in the toe domain and that strain within the fold-and-thrust  
20 belt varies laterally. This study shows that even minor horizontal translation of MTCs (c. 1 km) can  
21 drive marked lateral variability in frontal geometry and strain within the failed body, which may  
22 influence their seal potential in petroleum and carbon storage systems.

23 Mass-transport complexes (MTCs) are the deposits of creep, slide, slump, and debris flow processes  
24 (e.g. Dott 1963; Nardin et al. 1979; Nemeč 1991; Moscardelli & Wood 2008; Posamentier & Martinsen  
25 2011). MTC emplacement can cause major geohazards for offshore infrastructures and coastal  
26 communities (e.g. Tappin et al. 2001; Vanneste et al. 2013; Takagi et al. 2019) and can be an important  
27 component of a functional petroleum system (e.g. Weimer & Shipp 2004). For example, MTCs can  
28 provide seals for hydrocarbon accumulations (Algar et al. 2011; Omeru 2014; Cardona et al. 2016) and,  
29 less commonly, may act as reservoirs (Sawyer et al. 2007; Shanmugam 2012; Arfai et al. 2016). In  
30 particular, their seal potential depends on a combination of the lithology, external geometry and  
31 internal structural heterogeneity of the emplaced mass, which are all influenced by emplacement  
32 processes (e.g. Alves et al. 2014). Thus, it is important to understand their transport processes to  
33 assess their seal potential in a petroleum system.

34 The nature of the failed mass in the vicinity of the toewall defines two frontal geometrical types (Frey-  
35 Martínez et al. 2006): (i) frontally-confined types represent toewall trapping of a failed mass from  
36 further downdip translation, and (ii) frontally-emergent types reflect a failed mass that extends above  
37 and beyond the toewall with further translation onto the adjacent seabed. In some cases, both styles  
38 can develop within a single mass-transport event (Moernaut & De Batist 2011; Armandita et al. 2015;  
39 Clare et al. 2018). The seismic expression of both frontal termination types are well-known (Trincardi  
40 & Argnani 1990; Huvenne et al. 2002; Lastras et al. 2004; Joanne et al. 2013), but the processes  
41 occurring in the toe domain remain poorly constrained (e.g. evolution of the basal shear surface prior  
42 to termination at the toewall). Outcrop studies have provided detailed insights on processes in the  
43 toe domain, but a full 3D analysis is hindered by limited exposure extent (Martinsen & Bakken 1990;  
44 Van Der Merwe et al. 2011; Sobiesiak et al. 2016; Cardona et al. 2020). Furthermore, very few studies  
45 have attempted to balance extensional and contractional strains across the entire body of an MTC  
46 (e.g. Bull & Cartwright 2019; Steventon et al. 2019). Likewise, the way in which strain varies along-  
47 strike within an MTC remains poorly understood.

48 Here, we use high-resolution multibeam bathymetry and high-quality 3D seismic reflection data to  
49 study the Haya Slide (hereafter the 'slide'), offshore western Sulawesi (Indonesia). This dataset  
50 demonstrates how frontal toewall style can change laterally during emplacement of a single mass-  
51 transport event. The bathymetry data capture the seabed expression of both the headwall and toe  
52 domains of this slide, while the 3D seismic reflection data only image the toe domain, which is the  
53 focus of this study (Fig. 1). The seismic image quality and use of seismic attributes enable us to  
54 characterise intra-MTC strain in great detail. Our specific aims are to: (i) evaluate kinematic indicators  
55 and reconstruct transport processes of the slide, (ii) assess lateral variability of the slide's frontal  
56 geometry and infer its controlling factors, (iii) quantitatively examine along-strike changes of intra-  
57 MTC strain, and (iv) discuss how lateral variations in strain may impact the seal potential of MTCs.

## 58 **GEOLOGICAL SETTING**

59 The Makassar Strait is situated within an earthquake-prone region, where four major plates interact  
60 (the Eurasia, Indo-Australia, Philippine Sea, and Pacific plates; Fig. 1a) (Daly et al. 1991). A strong  
61 southwards-flowing current, the Indonesia Throughflow (ITF), presently carries water masses through  
62 the strait at a relatively high velocity (i.e. 1 m/s; Mayer & Damm 2012), from the Pacific Ocean to the  
63 Indian Ocean. Brackenridge et al. (2020) suggest that the ITF preconditions the slopes bounding the  
64 straits to fail, whereas earthquakes in this seismic-prone region may act as a trigger mechanism. More  
65 specifically, the ITF transports a high suspended sediment load southward from the Mahakam Delta,  
66 causing relatively rapid deposition and steepening of the continental slope along the western margin  
67 of the strait, which results in (i) slope oversteepening, and (ii) high pore-fluid pressures (Brackenridge  
68 et al. 2020). Such preconditioning factors for slope failure are consistent with the unusually large  
69 number of near-seabed MTCs (Pleistocene to Recent), which range in size from 5 to >600 km<sup>3</sup>  
70 (Brackenridge et al. 2020).

71 The Makassar Strait is located between the islands of Sulawesi and Kalimantan (Borneo) and is divided  
72 into the North and South Makassar basins (Fig. 1b). The water depth along the strait is 200-2000 m

73 (Guntoro 1999), with (i) a relatively broad, accretionary shelfal area along the western margin  
74 (including the Mahakam Delta; e.g. Allen & Chambers 1998), and (ii) a narrower and steeper shelf  
75 along the eastern margin, which is more tectonically active and bounded by three fold-thrust belts,  
76 namely the Northern (NSP), Central (CSP) and Southern (SSP) structural provinces (Puspita et al. 2005).  
77 These two marginal areas are the sources of the MTCs transported into the basins (Fig. 1c). The two  
78 basins are connected by the deep (c. 2000 m) and narrow (c. 45 km-wide) Labani Channel, and are cut  
79 by major structural features, such as the Palu-Koro and Paternoster transform fault zones (Cloke et al.  
80 1999) (Fig. 1b). We here focus on the Haya Slide (Fig. 1d), which is a shallowly buried MTC with only a  
81 thin (<8 m) veneer of modern sediment and a clear present-day seabed expression. The slide is located  
82 at the southern end of the Labani Channel, close to the southern margin of the SSP (Fig. 1b).

### 83 **DATA SET AND METHODOLOGY**

84 The study is based primarily on bathymetry, 3D seismic reflection and well data (Fig. 1b and d). TGS  
85 provided the multibeam echosounder bathymetry data (TGS\_Pat survey), which covers an area of c.  
86 20,000 km<sup>2</sup>. Lateral resolution of these data is 25 x 25 m and geomorphic features are enhanced by a  
87 shaded relief map with 0° azimuth and 45° angle. Core descriptions of near-seabed sediments (c. 3-7  
88 mbsf) are also available (i.e. TGS009 and TGS194, see Fig. 1b). Although none of these cores directly  
89 sample the Haya Slide, they enable the likely lithology of the slide to be inferred.

90 The post-stack time-migrated (PSTM) 3D seismic reflection and exploration well data (see Fig. 1b) are  
91 provided by the Information and Data Centre, Ministry of Energy and Mineral Resources (PUSDATIN  
92 ESDM), Indonesia. The seismic reflection data cover an area of 1598 km<sup>2</sup>, with a bin spacing of 25 m x  
93 12.5 m (inline x crossline) and a dominant frequency of 50 Hz at the base of the Haya Slide (c. 200  
94 mbsf). We estimate that the spatial resolution of the seismic data, given an average velocity of the  
95 sedimentary package of interest derived from the wells (1495 m/s), is c. 7 m. The average velocity of  
96 the near-seabed sediments is relatively low, likely due to the high water content. Similar values are  
97 obtained for near-seabed, deep-water sediments penetrated in the South Makassar MTC area, which  
98 is located c. 135 km to the SW of our study area (Armandita et al. 2015). The 3D seismic data are zero-

99 phase with SEG normal polarity with an increase in acoustic impedance expressed as a positive  
100 amplitude. The two wells (XR-1 and XS-1) do not penetrate the Haya Slide, and there are no drill  
101 cuttings data available, even within the general stratigraphic interval containing the slide. However,  
102 the correlation of the basal shear surface to the wells ('detachment level' in Fig. 1d) enables the  
103 velocity of the sedimentary package containing the slide to be inferred. Using these data allows the  
104 conversion of measured vertical distances in time (ms TWT) to depth (m).

105 The bathymetry data allow delineation of the external geometry of the slide (Fig. 2). These data also  
106 allow the headwall and a lateral margin (Eastern Lateral Margin, Fig. 2) of the slide to be determined  
107 (not covered by the 3D seismic reflection data). The 3D seismic reflection data cover most of the toe  
108 domain of the slide (Fig. 2). Mapping of the seabed and basal shear surface of the slide enables us to  
109 constrain the structural style of its toe domain and infer the processes occurring during transport and  
110 cessation of the slide. The following seismic attributes were used to visualise the range of intra-MTC  
111 structures: (i) *variance* – to show discontinuities such as imbricated thrusts (e.g. Chopra & Marfurt  
112 2007); and (ii) *spectral decomposition (RGB blending)* – to highlight heterogeneities of internal body  
113 of the slide by blending three bins of frequency volume with assigned colours (i.e. red, green and blue  
114 represent low, mid and high frequencies, respectively) (e.g. Partyka et al. 1999; Eckersley et al. 2018).  
115 We extracted these attributes along an iso-proportional slice (see Zeng et al. 1998) and horizontal  
116 time-slices, thereby generating map-view images of seismic facies and structural variability.

## 117 **THE HAYA SLIDE**

### 118 **General characteristics**

119 The Haya Slide is located c. 10 km off the coast of Sulawesi (Figs. 1 and 2). It is c. 16 km long, extending  
120 south-westwards from the lower slope (c. 1700 m below sea-level) to the basin floor (c. 2000 mbsl).  
121 The slide has a lobate geometry (Fig. 2): (i) it is c. 7 km wide in its headward region on the lower slope,  
122 (ii) widens to c. 15 km along its frontal margin in the centre of the basin floor, and (iii) it covers an area  
123 of 150 km<sup>2</sup>. The slide was derived from the southern flank of a thrust-cored anticline within the SSP.  
124 The anticline has a broadly arcuate trend and is dissected by the headwall of the slide (i.e. extending

125 from 1700 to 1900 mbsl (Fig. 2a). The external limits of the slide are defined as follows (Fig. 2): (i)  
126 Northern Lateral Margin, (ii) Eastern Lateral Margin, and (iii) Frontal Margin. This external geometry,  
127 including the inferred headwall erosion on the southern flank of the seabed anticline, indicates that  
128 the slide was emplaced towards the SW. Correlation with the laterally equivalent, slide-hosting  
129 package in wells XR-1 and XS-1 (Fig. 1d), confirms that the slide is located within the Quaternary. Cores  
130 from the slope (TGS009) and basin floor (TGS194) locations (Fig. 1b) indicate that (i) slope sediments  
131 are composed of clayey (fine to medium) sand, with low-medium cohesion and medium-high water  
132 content, and (ii) basin floor sediments are characterised by very soft to firm clay, with medium  
133 cohesion and medium-high water content.

134 The 3D seismic reflection data cover *c.* 78% of the slide, mainly covering its downdip portion and  
135 excluding the headwall region (see inset map in Fig. 3a). Thickness patterns (Fig. 3a) and frequency  
136 characteristics (Fig. 3b) display gradual variations in both strike and dip directions, which enable  
137 subdivision of the slide. Strike-oriented thickness variations highlight three distinct areas (Fig. 3a): (i)  
138 A (*c.* 170-200 m thick), (ii) B (*c.* 140-170 m), and (iii) C (*c.* 70-140 m). All three areas thin and wedge-  
139 out abruptly downdip, at approximately the same rate, towards the Frontal Margin. Area C also thins  
140 rapidly, at a similar rate, towards the Northern Lateral Margin that represents a boundary separating  
141 the downslope-translating slide and stationary substrate. Note that the Eastern Lateral Margin is  
142 inferred using bathymetry data alone, whereas the Northern Lateral Margin is imaged directly by the  
143 3D seismic reflection data.

144 Dip-oriented variations are defined by an isoproportional slice, taken midway between the basal shear  
145 surface and seabed (Fig. 3b), which shows frequency changes indicative of seismic facies and/or  
146 structural variability. The inner part of the slide is characterised by an overall lower RGB blend  
147 frequency and relatively short, discontinuous along-strike lineations. In contrast, outer areas display  
148 higher RGB blend frequency with longer, more continuous lineations, which extend across Areas A-C  
149 (Fig. 3b). These lineations predominantly trend E (090-270°) in the south (Area A) and N to NW (000-  
150 180°, 020-200°) in the west (Area C).

151 Three dip-oriented seismic sections across Areas A, B and C, oriented perpendicular to the curved  
152 lineations (Fig. 3b), define the internal character of the slide (Fig. 4a-c). These sections show that the  
153 inner part of the slide comprises chaotic, highly discontinuous, low-amplitudes reflections, which  
154 corresponds to the low RGB blend frequency seen in the spectral decomposition map (Fig. 3b). This  
155 seismic expression is typical of an internally disorganised and highly deformed debrite, as compared  
156 to other, drilled examples of MTCs (e.g. Piper et al. 1997; Posamentier & Martinsen 2011). Between  
157 the inner and outer parts, the isolated high RGB blend frequency bodies on Figure 3b (which dominate  
158 the outer part) correlate with isolated, folded, high-amplitude reflections encased within the inferred  
159 debrite (Fig. 4a-c). These bodies are interpreted as megaclasts, with their long axes oriented sub-  
160 parallel to the curved lineations (Jackson 2011; Alves 2015; Gamboa & Alves 2015; Hodgson et al.  
161 2018; Sobiesiak et al. 2018; Sobiesiak et al. 2019). The more continuous curved lineations in the outer  
162 part of the slide (Figure 3b) correspond to pairs of sharp discontinuities within the slide. These  
163 discontinuities converge downward onto the basal shear surface (e.g. Fig. 4a). We interpret these  
164 discontinuities as forethrusts (i.e. NE-dipping) and backthrusts (SW-dipping) that bound folded 'pop-  
165 up blocks' in their hangingwalls (e.g. Frey-Martínez et al. 2006; Bull & Cartwright 2019). The pop-up  
166 blocks (and their adjacent footwalls) are the lineation-bound, high RGB blend frequency bodies seen  
167 in map-view (Fig. 3b). Pop-up blocks are offset along-strike by discontinuities trending oblique (170°-  
168 350°) to the general trend of the bounding thrusts (Fig. 3b). These discontinuities are interpreted as  
169 sub-orthogonal shear zones (*sensu* Steventon et al. 2019) that may record boundaries between  
170 different flow-cells that moved at different speed within the translating failed mass (e.g. Masson et al.  
171 1993; Steventon et al. 2019). They are not interpreted as longitudinal shears (*sensu* Bull et al. 2009b)  
172 that are sub-parallel to the transport direction.

173 Although thrust-bound pop-up blocks typify the outer part of the slide, there are significant lateral  
174 variations (from Area A to Area C) in structural style and seismic facies characteristics, which are  
175 described below.



176 **Area A**

177 *Characteristics of Area A*

178 A gradual downslope-deepening of the basal shear surface characterises the base of the slide in Area  
179 A. The surface steps up to form a steep ramp (c. 60°) that defines the slide's frontal margin (Fig. 4a).  
180 The basal shear surface is deepest (c. 200 mbsf) adjacent to the frontal margin, with the basal shear  
181 surface essentially being horizontal. The upper surface of the slide is of low relief in the inner part,  
182 which may partly reflect the filling of top-surface relief by post-emplacement sedimentation (ponded  
183 sediments in Fig. 4a). The upper surface becomes more rugose down-dip and reaches its highest relief  
184 (15 m) at the frontal margin.

185 Seismic reflections in the outer part of the slide in Area A are well-imaged and can be directly  
186 correlated with undeformed strata beyond the frontal margin, despite being contractionally offset by  
187 thrust faults (Fig. 4a). The internal reflections of the slide become more irregular, and harder to trace,  
188 towards the inner part. In area A, the average throw and dip of the fore- and backthrusts are c. 30 m  
189 and c. 45°, respectively, with the spacing between thrust pairs (measured from crest to crest of pop-  
190 up blocks) ranging from 400 to 500 m.

191 *Interpretation of Area A*

192 The steep frontal ramp that separates undeformed basin-floor strata from the slide is a classic  
193 frontally-confined (*sensu* Frey-Martínez et al. 2006) termination style (Fig. 4a). Similar to previously  
194 documented frontally-confined MTCs, the thickness of the slide in the outer area (c. 200 m) is only  
195 expressed by minimal seabed relief at the edge of the deposit (c. 15 m) (e.g. Lastras et al. 2004; Frey-  
196 Martinez et al. 2005).

197 Internal reflections show higher preservation of stratal reflections in the outer than the inner parts,  
198 suggesting that the youngest thrust is located at the frontal margin of the slide (Fig. 4a), similar to  
199 those observed from outcrops (e.g. Alsop et al. 2019) and seismic reflection data (e.g. Frey-Martínez  
200 et al. 2006; Bull & Cartwright 2019). Physical modelling results suggest that regular spacing of fore-

201 and backthrusts is indicative of an MTC that was translated on a low friction basal shear surface (Huiqi  
202 et al. 1992).

## 203 **Area B**

### 204 *Characteristics of Area B*

205 Gradual downslope-deepening of the basal shear surface is also observed in Area B, with the surface  
206 progressively stepping up through stratigraphy to define three stepped levels of frontal ramp (Fig. 3a  
207 and Fig. 4b). The basal shear surface is deepest (c. 170 mbsf) immediately upslope from the first and  
208 deepest frontal ramp with the highest relief (30 m). The other two ramps are more gently-dipping and  
209 have lower relief (c. 20 m) (Fig. 4b). These three ramps truncate otherwise continuous, sub-parallel  
210 reflections defining the pre-slide substrate. The substrate in Area B dips very gently (c. 1°) in an  
211 opposing direction (i.e. north-eastwards) to the slide transport direction. The seabed in Area B is  
212 smooth but becomes more rugose downdip (Fig. 4b). Most notably, the highest seabed relief (c. 10 m)  
213 is located immediately above the deepest point of the basal shear surface.

214 The nature and distribution of the seismic facies in Area B differs from those of Area A, most notably  
215 a much higher level of reflection discontinuity. Also, the least disturbed strata (i.e. semi-continuous  
216 seismic reflections) occur in the central part of the slide, immediately upslope from the first frontal  
217 ramp. Directly above the frontal ramps, reflections are extremely chaotic with variable, higher  
218 amplitude seismic facies encased within more extensive transparent seismic intervals, which resemble  
219 those in the inner part (Fig. 4b). In the central area, where stratal reflections have the highest  
220 preservation, pop-up blocks and thrusts are geometrically similar to those in Area A. However, these  
221 pop-up blocks have a spacing of c. 150-300 m, which is about half that of Area A. Measuring the throw  
222 and dip of thrusts in Area B is harder than in Area A, likely due to seismic resolution limitations and  
223 the closer spacing of the thrusts. Where we can trace a marker horizon between thrust-bound pop-  
224 ups, the throw and dip of the thrusts are 49 m and 60°, respectively (i.e. similar to the maximum values  
225 observed in Area A).

226 A distinctive upstanding, undeformed block is identified on a variance timeslice and seismic section  
227 (see 'Intact block' in Fig. 5), which marks the transition between Area A and B. This block extends  
228 gradationally downwards into the undeformed slope-to-basinfloor strata (Fig. 5b), which continue  
229 unbroken towards the east. The block is bound (north and south) by the steep frontal ramp defining  
230 Area A and pop-up blocks within the toe domain of the slide (west and south). The block is capped by  
231 sub-parallel, variable-amplitude reflections, while further south it is bound by folded reflections that  
232 are cross-cut by minor thrusts. These thrusts detach onto a reflection that is stratigraphically shallower  
233 than the basal shear surface (Fig. 5b). We suggest that the basal shear surface steps up above this  
234 feature, before stepping down onto the reflection onto which the minor thrusts detach. The surface  
235 then steps up again to define the outermost frontal margin in Area B. Beyond this outermost frontal  
236 margin, a gently folded reflection is observed that probably marks the position where the next thrust  
237 would have formed (Frey-Martínez et al. 2006).

#### 238 *Interpretation of Area B*

239 The stepped geometry of the basal shear surface confining the slide in Area B argues against frontal  
240 emergence of the slide (Frey-Martínez et al. 2006). Seismic facies above the stepped frontal ramp  
241 comprise variable-amplitude, somewhat chaotic reflections that resemble debrites (*cf.* Posamentier  
242 & Kolla 2003; Ortiz-Karpf et al. 2017) (Fig. 4b). Pop-up blocks in Area B are located immediately updip  
243 from the frontal ramps (Fig. 4b). Here, the slide is thinner, and it contains more closely-spaced pop-  
244 up blocks than those in Area A. We therefore speculate that there might be a relationship between  
245 thickness and pop-up block width/thrust fault spacing. This is consistent with the physical and  
246 numerical modelling by Liu & Dixon (1995), who demonstrate a positive linear relationship between  
247 thrust spacing and thickness of the strata.

248 We interpret the intact block between Areas A and B as a piece of *in situ* substrate, based on its lack  
249 of deformation and gradational seismic facies relationship with underlying and adjacent basin floor  
250 strata. Hence, it can be interpreted as a remnant block (*sensu* Bull et al. 2009b). Minor thrusts downdip

251 from the remnant block suggest that there is a zone of relatively high strain beyond the main body of  
252 the slide (Fig. 5b). This zone of high strain could be a distributed shear zone, where compressional  
253 stress is transmitted beyond the frontal ramp (Hodgson et al. 2018). However, in those cases, the  
254 distributed shear zone is commonly in direct contact with the frontal margin of the main body (e.g.  
255 Watt et al. 2012). In our case, the remnant block exists in between two zones of relatively high strain  
256 (Fig. 5b). Therefore, an alternative interpretation is that the minor thrusts represent the lateral  
257 propagation of thrusts eastwards from Area C (Fig. 5a). This interpretation is plausible given that minor  
258 thrusts can be traced westwards on the variance time-slice, towards the main body of the slide (i.e.  
259 into Area C, Fig. 5a). The relationship between the main body of the slide, the remnant block, and the  
260 minor thrusts, partially resemble a process referred to as 'enveloping' (Hodgson et al. 2018). For  
261 example, a remnant block could form when an uneven frontal margin to the slide envelopes a large  
262 piece of substrate, but with the process terminating prior to complete entrainment of the block due  
263 to cessation of the slide's translation.

## 264 **Area C**

### 265 *Characteristics of Area C*

266 The basal shear surface in the outer part of Area C exhibits a similar geometry and internal  
267 characteristics to that of Area B, especially the staircase-like geometry of the basal shear surface (Fig.  
268 4c). However, the basal shear surface here is associated with a pronounced change in dip and dip  
269 direction, defined by a change from c. 1° basinward dip to a c. 3° landward dip (Figs. 4c and 6a). This  
270 change in dip coincides with the deepest (120 mbsf) occurrence of the basal shear surface. The seabed  
271 in Area C is characterised by a (i) c. 10 m vertical relief, and (ii) a c. 6 km long and 2 km wide 'bulge',  
272 immediately updip of the slide's frontal margin (Figs. 4c, 6b-c). Adjacent to the Northern Lateral  
273 Margin, the basal shear surface is relatively flat, and the seabed shows rugosity similar to that in Areas  
274 A and B, but with a shorter wavelength (Fig. 6d).

275 The internal characteristics of the slide in Area C, which resemble those in Area B, comprise the  
276 following: (i) chaotic reflections of variable amplitude encased within very low-amplitude reflections  
277 at the frontal margin, (ii) pop-up blocks within the slide's outer part, and (iii) megaclast-bearing  
278 debrites in the inner part (Fig. 4c). However, the pop-up blocks in Area C are more closely spaced (c.  
279 100-150 m) than those in Area B, which results in low stratal preservation in seismic sections (Fig. 4c).  
280 Thus, despite being well-imaged in map-view, from which pop-up blocks spacing can be measured  
281 (Fig. 3b), dip and throw measurements in Area C are uncertain (Fig. 4c). The frontal margin in Area C  
282 is characterised by rapid pinch-out of the slide's internal body onto the inclined (c. 3°) substrate (Fig.  
283 4c). Towards the Northern Lateral Margin, the spacing between pop-up blocks is even shorter (c. 70-  
284 100 m), and the basal shear surface is shallower (70 mbsf) (Figs. 3 and 6d). Near the frontal margin,  
285 sub-parallel, discontinuous, high-amplitude reflections occur between the basal shear surface and the  
286 largely transparent seismic facies defining the main body of the slide (Fig. 4c). These reflections are  
287 correlated with a c. 25 m-thick interval located basinward of the slide, comprising inclined, largely  
288 undeformed, reflections (Fig. 4c).

289 The boundary between Areas B and C comprises a NE-trending/NW-facing ramp, which is laterally  
290 continuous with the NW-trending/NE-facing frontal ramp of Area B (Fig. 7a). Variance attributes  
291 extracted from a 50 ms TWT thick window above the basal shear surface show several NW-trending  
292 lineations that terminate against the NE-trending ramp. In seismic section, these lineations  
293 correspond to fold-and-thrust belt structures in Area C (Fig. 7b). Thus, the NE-trending ramp forms a  
294 boundary between the fold-and-thrust system and the undeformed substrate. The NE-trending ramp  
295 also coincides with a positive relief on the seabed.

#### 296 *Interpretation of Area C*

297 The slope gradient break at the basal shear surface and emergent of the leading-edge part of the slide  
298 that onlaps onto the underlying inclined substrate are likely to be related. We suggest that the physical  
299 impact of the downslope-translating slide onto its substrate was highest where the basal shear surface

300 abruptly changes dip and dip direction (Ogata et al. 2014b). Following this impact, variations in the  
301 mechanical properties of the substrate likely controlled the morphology of the basal shear surface  
302 (Strachan 2002; Frey-Martinez et al. 2005; Moernaut & De Batist 2011). For instance, substrates with  
303 higher shear strengths (e.g. due to lower pore-pressure) force the basal shear surface to step-up to  
304 shallower substrates and propagate along inclined substrates that have lower shear strength (Fig. 4c).  
305 The inclined basal shear surface and momentum gained by the slide at the dip change provide  
306 sufficient inertial energy for the translating mass to abandon the basal shear surface and emerge onto  
307 the coeval basin floor, and to onlap the bathymetric high (Figs. 4c, 6b) (Frey-Martinez et al. 2005; Frey-  
308 Martínez et al. 2006). Therefore, we classify the slide in Area C as frontally-emergent (*sensu* Frey-  
309 Martínez et al. 2006). However, the slide also becomes frontally-confined adjacent to the Northern  
310 Lateral Margin, where the slide is thin, and the basal shear surface is relatively flat and lacks a distinct  
311 dip change (Fig. 6d; *cf.* Area A in Fig. 4a).

312 The abrupt change in basal shear surface dip has at least two additional consequences. Firstly, the  
313 internal body of the slide was likely disaggregated due to the buttressing effect of the underlying  
314 substrate (Mandl & Crans 1981). This resulted in the partially-disaggregated debrite facies in the  
315 frontal margin area, which is manifested as the broad bulge on the seabed (Fig. 6b-c). Secondly, the  
316 impact of the translating mass onto the substrate develops a zone of stratigraphically parallel,  
317 discontinuous reflections directly on top of the basal shear surface (e.g. Joanne et al. 2013). We  
318 interpret these reflections as lying within the basal shear zone, in which the substrate was deformed  
319 due to compressional forces exerted by the slide, but was not fully entrained (e.g. Hodgson et al. 2018;  
320 Cardona et al. 2020).

321 The abrupt boundary between Areas B and C indicates that the basal shear surface evolved differently  
322 between the two areas, where the frontal ramp of Area B was cross-cut by the main body in Area C  
323 (Fig. 7a). This cross-cutting relationship probably formed by the slide's cannibalisation of the substrate  
324 in Area C, which formed the NW-facing ramp (Fig. 7a-b). Lateral variations in basal shear surface

325 growth and geometry could also be related to lateral variations in the mechanical properties of the  
326 stratigraphy overlying the basal shear surface (e.g. permeability, pore-pressure and related shear  
327 strength). In addition, variations in the magnitude of stress exerted by the slide onto, and into, the  
328 substrate in adjacent areas may have occurred (Strachan 2002; Frey-Martinez et al. 2005). Positive  
329 seabed relief adjacent to the NE-trending ramp likely reflects a buttressing effect of the main body of  
330 the slide against the ramp as new material was entrained by the slide (Fig. 7b).

### 331 **Estimation of translation distance and along-strike variability of strain in the toe domain**

332 We here estimate the translation distance of the Haya Slide based on an assessment of shortening  
333 within Area A that has the best preservation of internal reflections. We also quantify intra-MTC strain  
334 of a pop-up block within Area A to investigate how strain varies along strike.

#### 335 *Shortening strain and its relationship to translation distance*

336 The distance travelled by the slide where frontally confined can be estimated by measuring total  
337 shortening in the toe domain, as long as the fold-and-thrust belts and the internal reflections are well-  
338 preserved and imaged (*cf.* Frey-Martínez et al. 2006; Bull & Cartwright 2019). We note that the  
339 calculated translation distance here is a first-degree estimation of how far the slide has travelled in  
340 the toe domain (Frey-Martínez et al. 2006), and, thus, it does not represent run-out distance, which is  
341 measured from the headwall to the leading-edge of the deposit (Clare et al. 2018). We note that the  
342 estimated shortening values would underestimate intra-MTC strain (i.e. minimum value), as the line-  
343 length method does not account for shortening within pop-up blocks due to sub-seismic strain, lateral  
344 compaction accommodated by porosity loss via dewatering, and/or grain crushing (Moore et al. 2011;  
345 Armandita et al. 2015; Alsop et al. 2019; Steventon et al. 2019).

346 A representative depth-converted seismic-section in Area A (interval velocity derived from wells XR-1  
347 and XS-1) was selected for our shortening calculation based line-length method (see Figs. 3b and 4a).  
348 This section is orientated perpendicular to the strike of the fold-and-thrust belt, and stratal reflections  
349 within individual thrust-bound blocks are well-imaged, and can thus be interpreted with confidence.

350 Two intra-MTC horizons were interpreted (H1-2, see Fig. 4a) to better constrain the amount of  
351 horizontal shortening and to determine how this varies vertically. These horizons extend from  
352 undeformed basin-floor strata to the updip limit of the outer part (Fig. 4a). The present and restored  
353 lengths of H1, the deepest horizon, are 6.73 km and 7.79 km, respectively, which equate to 14%  
354 contraction (1.06 km). In contrast, the shallower H2 horizon experienced only 8% contraction (0.61  
355 km), derived from present and initial lengths of 6.65 km and 7.26 km, respectively. This analysis shows  
356 two key results: (i) contractional structures in Area A (Fig. 4a) formed in response to horizontal  
357 translation of the slide over a relatively short distance (0.61-1.06 km), and (ii) greater contraction of  
358 the deeper H1 horizon compared to the shallower H2 indicates depth-dependent layer shortening due  
359 to penetrative strain (e.g. thickening and partial area loss of deeper layer, Koyi 1995).

#### 360 *Along-strike variability of intra-MTC strain*

361 An along-strike analysis enables the kinematics behind the spatial configuration of fold-and-thrust  
362 belts to be assessed (Dahlstrom 1969). Such studies have been performed for kilometre-scale, deep-  
363 water fold-and-thrust belts using 3D seismic reflection data (e.g. Higgins et al. 2009; Totake et al.  
364 2018). Here, we document the along-strike variability of intra-MTC strain at a significantly smaller-  
365 scale, but exceptionally well-imaged, fold-thrust system within the Haya Slide.

366 We conducted the along-strike analysis on Pop-up Block 3 (i.e. the third block counted from the frontal  
367 margin, and herein referred to as PB-3; see Fig. 4a) and its associated fore- and backthrusts. This pop-  
368 up block is ideal for this analysis because its main bounding thrust fault (FT-1) and Horizon H2 can be  
369 interpreted over the longest distance (c. 3 km along strike, see Fig. 8a); other pop-up blocks are shorter  
370 and more segmented along strike (c. 0.5-1 km). We measured throw along the fore- (FT) and  
371 backthrusts (BT) at intervals of 20-200 m. The throw was measured because most thrusts dip 40°-60°  
372 and strain is better quantified by measuring throw, rather than heave that diminishes with increasing  
373 dip (Totake et al. 2018).



374 Mapping of H2 laterally from the representative section of Area A (i.e. Fig. 4a) reveals a more  
375 complicated configuration of pop-up structures associated with PB-3; whereas there is only a single  
376 pop-up in the east (PB-3a), there are two in the west (PB-3b-c; Fig. 8a). These three pop-up blocks are  
377 readily identified on a variance time-slice (Fig. 8b). Here, one of the sub-orthogonal shear zones  
378 identified in the previous section (see General Characteristics and white dotted lines in Fig. 3b), trends  
379 oblique to, and cross-cuts, the thrust faults near the central part of the focused study area (white  
380 dotted line in Fig. 8b). This shear zone clearly defines the boundary between PB-3a in the east and PB-  
381 3b and c in the west (Fig. 8a).

382 The structural configuration is seen on both the H2 time-structure map and variance time-slice (Fig.  
383 8a-b). At the shear zone, the southern margin of the PB-3a and b shows an 80 m left-lateral (sinistral)  
384 offset (Fig. 8b). Therefore, the translated mass to the west appeared to travel downdip only a small  
385 amount further than the mass to the east when compared to the overall estimated translation  
386 distance of the slide (i.e. 7.5-13% of 0.61-1.06 km translation distance). PB-3a is bound on its northern  
387 margin by one major backthrust (BT-1), and one minor FT-2 exists adjacent to FT-1. In contrast, PB-3b  
388 is bound on its northern side by BT-2 and -3 that forms a 'soft-linkage' with each other (*sensu* Walsh  
389 & Watterson 1991). Unlike PB-3a and -b, PB-3c is not bound by FT-1, but is instead bound by two  
390 forethrusts (FT-4 and FT-5) and two backthrusts (BT-4 and BT-5). BT-1 and BT-4 are soft-linked (near  
391 the shear zone) and bound limit the northern margin of PB-3a and c, respectively, (Fig. 8a). The faults  
392 bounding the three pop-up structures generally strike E-W to ESE-WNW. In addition to the faults that  
393 define PB-3a-c, we identify two faults (i.e. FT-3 and BT-6) within the shear zone (Fig. 8a-b). These faults  
394 bound a narrow (c. 100 m-wide), uplifted block that may have formed due to transpression within the  
395 shear zone (Sanderson & Marchini 1984).

396 Throw profiles of individual fore- and backthrust faults show multiple maxima and minima (Fig. 8c),  
397 resembling larger, tectonic-scale fold-thrust systems, such as in offshore NW Borneo (Totake et al.  
398 2018) and Niger Delta (Higgins et al. 2009). T-x plot of FT-1 shows that it has a slightly lower throw (c.

399 5-10 m) in the western (PB-3b) than in the eastern (PB-3a) domains (Fig. 8c). This contrasts with an  
400 increase of the number of thrusts, resulting in a significantly higher cumulative throw: from c. 20-40  
401 m in the E to c. 40-60 m in the W (Fig. 8c). This might indicate that pop-up structures in the western  
402 domain are in a more advanced phase of growth (e.g. Cartwright et al. 1995; Totake et al. 2018). A  
403 local minima in the cumulative throw profile, which coincides with the local minima of FT-3, marks the  
404 boundary between the eastern and western domains (Fig. 8c). This boundary may represent a paleo-  
405 linkage site (Ellis & Dunlap 1988), which in this study coincides with the shear zone (Fig. 8a-b). The  
406 seismic sections across PB-3 depict the change in the fold-and-thrust configuration along strike (Fig.  
407 8d-f), from the eastern area, the shear zone, to the western area.

408 We found two different strain domains within the translated mass: in the eastern and western  
409 domains, separated by an intra-MTC, syn-emplacement shear zone (Fig. 8a-b). These two domains  
410 were likely transported a similar distance. However, they experienced significantly different amounts  
411 of contraction, as evidenced by the cumulative throw profile (Fig. 8c). Several studies show that  
412 internal shear zone reflects differential timing or velocities of translating masses (or 'cells') within an  
413 MTC (Masson et al. 1993; Gee et al. 2005; Bull et al. 2009a; Steventon et al. 2019). It implies that a cell  
414 that is transported for a longer duration, or at a higher velocity, would likely travel further. We show  
415 here that when the intra-MTC cells could not travel further due to frontal confinement of the failed  
416 mass, stress imposed by still-moving material towards its rear can be accommodated by the formation  
417 of additional/larger contractional structures (e.g. folds and thrust faults). This process results in along-  
418 strike variability in the style and magnitude of intra-MTC strain, with the shear zone separating the  
419 intra-MTC cells recording the different amounts of strain.

## 420 **DISCUSSION**

421 We here discuss the slide transport processes and lateral variability of frontal emplacement and intra-  
422 MTC strain within the toe domain. Also, we discuss the implications for assessing the seal potential of  
423 MTCs in relation to hydrocarbon accumulations.

424 **Modes of transport**

425 Frey-Martínez et al. (2006) show the headwall domain of frontally-confined MTCs are defined by  
426 internally coherent, normal fault-bound blocks. In this domain, there is only limited depletion of the  
427 failed mass immediately downdip of the headwall. However, more recent studies show that major  
428 sediment depletion in the headwall domain can occur even if the MTCs are frontally confined (e.g.  
429 Lastras et al. 2004; Watt et al. 2012; Joanne et al. 2013). In such cases, these frontally-confined MTCs  
430 are generally characterised by strongly disaggregated, debritic material in their inner parts, rather  
431 than fault-bound blocks. Downdip, contractional structures (e.g. folds and imbricated thrusts) display  
432 increasing stratal preservation distally.

433 The Haya Slide comprises an inner, debrite-dominated part and an outer part dominated by  
434 contractional structures. The debrite likely originated from the collapse of the southern flank of an  
435 updip anticline (see Fig. 3). This deformed the seabed and entrained the substrate (Fig. 9a), which  
436 resulted in flow bulking further downslope (Gee et al. 2001; Butler & McCaffrey 2010). Substrate  
437 entrainment and subsequent downslope translation then produced transparent seismic facies (i.e. the  
438 debrite in Fig. 4), indicating that the incorporated material was increasingly disaggregated  
439 (Posamentier & Kolla 2003; Ortiz-Karpf et al. 2017). Erosion and disaggregation by the debris flow  
440 continued until the shear stress exerted by the flow was unable to entrain more substrate (Fig. 9b). At  
441 this point, the debris flow applied significant shear and compressional stress (lateral loading) to the  
442 substrate ahead of, and to the sides of, the flow (Butler & McCaffrey 2010; Hodgson et al. 2018).

443 The strata ahead of the debris flow were translated a short distance (i.e. 0.61-1.06 km), forming  
444 broadly symmetrical pairs of fore- and backthrusts (Fig. 9c). This symmetrical geometry of the thrusts  
445 is likely due to low basal friction during shearing (Huiqi et al. 1992). The low basal friction may reflect  
446 the fact that the failed mass had a high water content, and thus high pore pressure (e.g. Armandita et  
447 al. 2015). The two styles of MTC-substrate interactions, i.e. erosion and deformation (Fig. 9c), have  
448 been documented elsewhere, both in seismic reflection (e.g. Schnellmann et al. 2005; Watt et al. 2012;

449 Joanne et al. 2013; Ogata et al. 2014a; Bull & Cartwright 2019; Omeru & Cartwright 2019; Steventon  
450 et al. 2019), and field data (e.g. Van Der Merwe et al. 2011; Sobiesiak et al. 2016; Sobiesiak et al. 2019;  
451 Cardona et al. 2020). Adjacent to the toewall, the basal shear surface evolves differently along strike  
452 (Fig. 10), which will be discussed in the following section.

### 453 **Lateral variability of the toe domain**

#### 454 *Lateral variability of frontal confinement*

455 Moernaut & De Batist (2011) investigated sub-lacustrine MTCs to understand what controls whether  
456 an MTC remains confined, or whether it abandons its basal shear surface and emerges onto the coeval  
457 basin floor. They conclude that the drop height and depth of the basal shear surface are the main  
458 factors controlling frontal emplacement style. The former represents a driving force (i.e. gravitational  
459 potential energy), and the latter represents a resisting force (i.e. potential energy needed to be  
460 exceeded for the MTC to emerge).

461 The Haya Slide originated from a headwall at a depth of c. 1700 mbsl, and its frontal margin is at c.  
462 2000 mbsl (the basinward extent of Areas A to C) (see Fig. 3). Thus, the drop height of the slide is 300  
463 m, which provided a similar driving force (potential energy) for all the three frontal areas. However,  
464 the depth of the basal shear surface, and thus the thickness of the slide, varies laterally: it is deepest  
465 in Area A (c. 200 mbsf) and shallowest in Area C (c. 120 mbsf). This lateral variability of basal shear  
466 surface depth, slide thickness and degree of confinement must also reflect lateral changes in the ratio  
467 between the resisting and driving forces (Fig. 10). In particular, the driving forces needed for the slide's  
468 emergence in Area A were greater than that in Area C. Therefore, the Haya Slide exhibits a lateral  
469 variation of frontal emplacement (Fig. 10); i.e. full frontal confinement in Area A, partial confinement  
470 across several staircase-like frontal ramps in Area B, to frontal emergence in Area C. Lateral friction  
471 along the Northern Lateral Margin may have also locally increased the resisting force in addition to  
472 the basal friction (e.g. Joanne et al. 2013), such that the slide is frontally-confined in that area despite  
473 being at its thinnest (Fig. 6d).

474 There is also a broad correlation between the basal shear surface morphology (i.e. depth and slope  
475 gradient break) and the overlying structural style in the toe domain. In Area A, for example, a relatively  
476 flat gradient, coupled with a deep basal shear surface, is associated with a steep (c. 60°) frontal margin  
477 (Figs. 4a and 10). This steep frontal margin represents the youngest forethrust that was formed as the  
478 slide ceased to translate (Fig. 11a) (e.g. Watt et al. 2012; Joanne et al. 2013; Alsop et al. 2019). In  
479 contrast, Area C displays a low-angle (3°), upslope-dipping, and relatively shallow basal shear surface  
480 related to the frontal ramp and slide emergence onto the coeval basin floor (Figs. 4c and 10). Here, a  
481 bathymetric high (see Fig. 6a-c) that existed prior to slide emplacement formed inclined strata ahead  
482 of the slide. This inclination increased the impact of the slide onto the substrate. The increased impact  
483 led to: (i) the formation of basal shear zone, and (ii) allowed the slide to transfer remaining exerted  
484 stress by abandoning the basal shear surface and translate on the coeval seafloor (Fig. 11b). Such distal  
485 bathymetric confinement has also been documented elsewhere, for instance, in offshore Colombia,  
486 where channel-levee morphology could deflect and/or block debris flows (Ortiz-Karpp et al. 2017).

487 Areas A and C represent end-member styles of the sub-slide basal shear surfaces. Morphologically,  
488 the basal shear surface in Area B lies between Areas A and C, being defined by a low-angle (1°) surface,  
489 an intermediate-depth and a staircase-like set of frontal ramps (Fig. 4b and 10). The formation of these  
490 ramps can be compared to the ramps and flats present along non-planar thrust faults, where the  
491 ramps tend to form in relatively high-shear strength layers, and the flats (e.g. basal shear surface  
492 connecting the ramps) in weaker layers (Fossen 2016). The potential energy of the slide in Area B  
493 might have been progressively (rather than instantaneously) dissipated in the distal area (Fig. 11c).  
494 Here, the basal shear surface may have propagated downslope along a horizon until it encountered a  
495 layer with higher shear strength (i.e. the red point in Fig. 11c). At that point, the basal shear surface  
496 stepped-up through stratigraphy and continued to propagate in shallower levels (i.e. initiated from  
497 the green point in Fig. 11c). This process might have continued several times to form the staircase-like  
498 frontal ramps, eventually terminating when the shear strength of the strata ahead of the flow  
499 exceeded the shear stress exerted by the slide (Fig. 11c). Alternatively, the staircase-like geometry

500 might represent a transitional style between full frontal confinement and full frontal emergence. The  
501 first frontal ramp in Area B links along-strike to the frontal ramp in Area A (Fig. 3a). Thus, this first step  
502 can be interpreted as the initial toewall. However, this initial toewall was not developed to form a  
503 steep ramp such as that in Area A. Instead, the debrite-like seismic facies above the subsequent steps  
504 might represent a style of frontal emergence (Fig. 4b). Consequently, the slide must have abandoned  
505 the basal shear surface, and progressively shallowed and incorporated material downdip from the  
506 initial toewall. This differs to Area C where the slide expelled material on to the coeval basin floor.

507 There is also some degree of correlation between the depth of the basal shear surface and the degree  
508 of disaggregation adjacent to the toewall. In Area A, where the basal shear surface is deeply-rooted,  
509 internal reflections of the slide are well-preserved (Fig. 11a). In contrast, in Areas B and C, where the  
510 basal shear surface progressively shallows, internal reflections of the slide exhibit debritic facies,  
511 indicating internal disaggregation (Fig. 11b-c). A similar relationship has also been documented in the  
512 thinner part of MTCs in offshore Brazil (Alves & Cartwright 2009; Gamboa et al. 2011) and offshore  
513 Colombia (Ortiz-Karpf et al. 2017). These studies conclude that the shallowing basal shear surface led  
514 to an increase in shear stress at the base of the flow with increased disaggregation.

515 Hence, we conclude that the interplay between stresses exerted by parent flow and variation of  
516 mechanical properties of the sedimentary package (both locally and regionally), controls the  
517 morphology of the basal shear surface (Figs. 10 and 11) (Bull et al. 2009b; Shanmugam 2015; Hodgson  
518 et al. 2018; Sobiesiak et al. 2018).

#### 519 *Lateral variability of intra-MTC strain*

520 Only a few studies have used seismic reflection data to quantify intra-MTC strain (Bull & Cartwright  
521 2019; Steventon et al. 2019). More specifically, these studies have focused on: (i) strain balancing  
522 between headwall and toe domains of MTC located offshore Uruguay (Steventon et al. 2019) and  
523 offshore Norway (i.e. Confined Storoegga Slide (CSS), Bull & Cartwright 2019); and (ii) assessment of  
524 depth-dependant layer shortening in the toe domain (Steventon et al. 2019). The Uruguay example

525 shows that contractional strain in the toe domain is apparently greater than (by *c.* 3-14%), and thus  
526 does not balance, extensional strain in the headwall domain (Steventon et al. 2019). This strain deficit  
527 is attributed to sub-seismic penetrative strain, likely associated with grain-scale deformation, and  
528 porosity and fluid loss (Koyi 1995; Koyi et al. 2004; Burberry 2015; Dalton et al. 2017; Alsop et al. 2019).  
529 In contrast, the study of the CSS found that extensive sediment depletion in the headwall domain is  
530 accommodated by only relatively mild contraction (*c.* 5%) in the toe domain (Bull & Cartwright 2019).  
531 This discrepancy is inferred to reflect a subsequent phase of deformation that involved the removal  
532 of a significant amount of material from the headwall domain after emplacement of the CSS.

533 Besides longitudinal balancing of MTCs, seismic-scale vertical variability of intra-MTC strain has also  
534 been documented. Steventon et al. (2019) documented that the deeper horizon (i.e. closer to the  
535 basal shear surface) experienced more shortening (*c.* 27%) than the shallower horizons (*c.* 18%) in the  
536 toe domain of the MTC, offshore Uruguay. We find similar results in the Haya Slide, where deeper (H1)  
537 and shallower (H2) horizons record *c.* 14% and *c.* 8% of shortening, respectively (Fig. 4a). These  
538 observations suggest that the magnitude of shortening estimate depends on the measurement depth  
539 due to depth-dependant horizontal shortening, with strain being greatest at depth. Physical models  
540 of horizontal shortening suggest that the increase of shortening with depth is balanced by bed-length  
541 decrease, lateral compaction of deeper layers, layer-normal thickening of shallower layers, and  
542 increased thrust displacement (Koyi 1995; Koyi et al. 2004; Burberry 2015). One or a combination of  
543 these processes might occur within the toe domain of a seismic-scale MTC.

544 The examples above show that intra-MTC strain varies both longitudinally and vertically. Our along-  
545 strike analysis of PB-3 and its associated thrusts indicate that intra-MTC strain also varies laterally,  
546 with a shear zone separating two regimes of contraction within a translated mass (Fig. 8). This  
547 represents a seismic-scale example of the field data-derived, multi-cell flow model of Alsop & Marco  
548 (2014) (see also Farrell 1984). This model states that a first-order, single-cell MTC is composed of many  
549 smaller, second-order flow cells that are formed during translation and may locally interact (Alsop &

550 Marco 2014). This local interaction is revealed by our along-strike analysis of PB-3, which we infer is  
551 contained within a more extensive, first-order cell. The eastern and western domains of the pop-up  
552 block represent second-order flow cells, with the shear zone representing the flow cell boundary. In  
553 the context of multi-cell flow model, PB-3 might initially have been a single body (or cell) of sediment,  
554 experiencing the same amount of stress laterally. However, velocity perturbations during translation  
555 of the first-order cell, perhaps due to variable basal shear stress, initiated the formation of the shear  
556 zone and caused formation of the two second-order flow cells within the initially continuous pop-up  
557 block. The western cell may have been translated at a faster speed than the eastern cell, so that the  
558 western cell records a more advanced stage of contraction than the eastern one.

#### 559 **Impact of intra-MTC strain on seal potential**

560 MTCs can play at least two roles in the development of petroleum systems: (i) commonly as seals  
561 (Algar et al. 2011, Cardona et al. 2016), and (ii) rarely as reservoirs (Sawyer et al. 2007; Algar et al.  
562 2011; Shanmugam 2012; Arfai et al. 2016; Cardona et al. 2016). This is controlled by three key  
563 parameters: (i) provenance lithology, most notably sand/mud ratio (Jenner et al. 2007; Omosanya &  
564 Alves 2013), (ii) substrate lithology and erodibility (Cardona et al. 2020), and (iii) the degree of internal  
565 disaggregation (Alves et al. 2014), which may include significant permeability reduction (2.5-3.5 orders  
566 of magnitude) due to grain crushing in otherwise good quality reservoirs (Crawford 1998). A strongly  
567 disaggregated (e.g. debrite-dominated) MTC derived from a very-fined grained source may result in  
568 high seal potential (Alves et al. 2014; Omeru 2014; Cardona et al. 2016). However, this may be  
569 compromised by entrainment of coarser-grained substrate and/or by the presence of rafted blocks  
570 (megaclasts) with reservoir potential (Gamboa & Alves 2015; Cardona et al. 2016; Cardona et al. 2020).  
571 Hence, substrate entrainment may result in (i) increased permeability and thus lower overall seal  
572 capacity, and/or (ii) localized high-permeability zones that can promote vertical fluid migration and  
573 hydrocarbon leakage.



574 Seal competence can vary longitudinally, from head to toe domains of the MTC, due to substrate  
575 entrainment and shearing during transport (e.g. Cardona et al. 2020). The Haya Slide is a clay-rich MTC  
576 that contains debritic facies in the inner part; this area may therefore represent a good hydrocarbon  
577 seal when compared to the imbricated, but otherwise internally moderately undeformed blocks  
578 present in the outer part (Figs. 3b and 4). However, we also document notable along-strike variations  
579 in seismic facies in the outer part (Fig. 4). For instance, Area A is characterised by imbricated thrusts.  
580 If these thrusts lack clay smear and are relatively permeable compared to the flanking, very fine-  
581 grained host rock, they may be conduits for fluid migration, implying a higher seal risk for this area  
582 (i.e. low seal potential). Towards Area C, seismic facies become more chaotic and transparent,  
583 suggesting a higher degree of deformation and internal disaggregation. Seismic facies in Area C may  
584 thus suggest a better seal potential here than in Area A because chaotic and transparent seismic facies  
585 have higher seal potential than blocky MTCs containing preserved stratigraphy (Alves et al. 2014;  
586 Omeru 2014). Therefore, our results suggest that seal potential of an MTC can vary along both  
587 depositional dip and strike within any one domain. The results presented here could be used to inform  
588 prediction of seal potential in MTCs at deeper, economic burial depths.

## 589 **CONCLUSIONS**

590 A recent mass-transport complex (MTC), the Haya Slide, has been characterised in the Makassar Strait  
591 based on high-quality 3D seismic reflection and bathymetry data. The slide originated from the  
592 collapsed flank of an anticline in the NE and transported radially to the SW. An along-strike analysis of  
593 the toe domain of the slide has provided the following conclusions concerning lateral variability of  
594 frontal emplacement and intra-MTC strain distribution:

- 595 1. The inner part of the toe domain is characterised by a debrite, which passes, first, downdip  
596 into megaclast-bearing debrite and, second, into coherent pop-up blocks towards the outer  
597 part. The debrite and the pop-up blocks are genetically-related, sharing the same bounding  
598 surfaces. Lateral loading by the debrite onto coherent strata induced progressive downslope

599 failure. Shortening estimates across the coherent strata show 8-14% of shortening, equating  
600 to 0.6-1.1 km of downslope translation.

601 2. The outer part of the toe domain exhibits the following lateral variability: (i) depth and  
602 gradient of the basal shear surface, (ii) trend and spacing of the pop-up blocks and their  
603 associated thrust faults, and (iii) frontal emplacement processes. A deep and relatively flat  
604 basal shear surface is associated with frontal confinement, where steep ramp separates  
605 undeformed strata and the slide. A shallow and upflow-dipping basal shear surface is  
606 associated with frontal emergence of the slide onto the coeval basin floor. Between these two  
607 extremes, the frontal geometry is characterised by staircase-like frontal ramps. Internal  
608 architecture of the slide may also be related to the geometry of the basal shear surface, where  
609 highly disaggregated material can be associated with the progressive shallowing basal shear  
610 surface. The interplay between drop height (i.e. driving force),= and along-strike depth  
611 variation of basal shear surface (i.e. resistive force),= likely to determine the lateral variability  
612 of frontal geometry of the slide. For instance, where resistive force < driving force led to  
613 frontal emergence, otherwise the slide would be frontally confined.

614 3. A detailed study of fold-and-thrust structures within the region of pop-up block shows along-  
615 strike variability of intra-MTC strain. This shows western and eastern regions of the toe  
616 domain, separated by a shear zone, experiencing different amounts of contraction. The  
617 western regime records a higher amount of strain, reflecting a more advanced phase of  
618 structural growth compared to its eastern counterpart.

619 4. Previous studies have shown that an MTC could have variable seal competence based on its  
620 axial domains (headwall to toe) due to different degree of disaggregation and substrate  
621 entrainment. The Haya Slide shows not only that, but there are also distinctive along-strike  
622 variations, which could influence seal potential predictions in petroleum systems.

623 **ACKNOWLEDGEMENT**

624 We thank Information and Data Centre, Ministry of Energy and Mineral Resources (PUSDATIN ESDM)  
625 Indonesia for providing 3D seismic reflection and well data (No. 015/Pj/05/SJD.2/2018), and TGS for  
626 providing multibeam bathymetry and near-seabed core data. Schlumberger, Geoteric and Midland  
627 Valley Exploration for granting software licences to Imperial College London. The first author thanks  
628 the Indonesia Endowment Fund for Education (LPDP) (Grant No.: 20160822019161) for its financial  
629 support.

630 **CONFLICT OF INTEREST**

631 No conflict of interest declared.

632 **REFERENCES**

- 633 Algar, S., Milton, C., Upshall, H., Roestenburg, J. & Crevello, P. 2011. Mass-transport deposits of the  
634 deepwater northwestern Borneo margin - Characterization from seismic-reflection, borehole, and  
635 core data with implications for hydrocarbon exploration and exploitation. *Mass-transport deposits in*  
636 *deepwater settings: Society for Sedimentary Geology (SEPM) Special Publication 96*, 7-38.
- 637  
638 Allen, G.P. & Chambers, J.L. 1998. *Sedimentation in the modern and Miocene Mahakam Delta*.  
639 Indonesian Petroleum Association, Jakarta.
- 640  
641 Alsop, G.I. & Marco, S. 2014. Fold and fabric relationships in temporally and spatially evolving slump  
642 systems: A multi-cell flow model. *Journal of Structural Geology*, **63**, 27-49.
- 643  
644 Alsop, G.I., Weinberger, R., Marco, S. & Levi, T. 2019. Fold and Thrust Systems in Mass-Transport  
645 Deposits Around the Dead Sea Basin. *Submarine Landslides: Subaqueous Mass Transport Deposits*  
646 *from Outcrops to Seismic Profiles*, 139-153.
- 647  
648 Alves, T.M. 2015. Submarine slide blocks and associated soft-sediment deformation in deep-water  
649 basins: A review. *Marine and Petroleum Geology*, **67**, 262-285.
- 650  
651 Alves, T.M. & Cartwright, J.A. 2009. Volume balance of a submarine landslide in the Espírito Santo  
652 Basin, offshore Brazil: Quantifying seafloor erosion, sediment accumulation and depletion. *Earth and*  
653 *Planetary Science Letters*, **288**, 572-580, <http://doi.org/10.1016/j.epsl.2009.10.020>.
- 654  
655 Alves, T.M., Kurtev, K., Moore, G.F. & Strasser, M. 2014. Assessing the internal character, reservoir  
656 potential, and seal competence of mass-transport deposits using seismic texture: A geophysical and  
657 petrophysical approach. *AAPG Bulletin*, **98**, 793-824, <http://doi.org/10.1306/09121313117>.
- 658  
659 Arfai, J., Lutz, R., Franke, D., Gaedicke, C. & Kley, J. 2016. Mass-transport deposits and reservoir quality  
660 of Upper Cretaceous Chalk within the German Central Graben, North Sea. *International Journal of*  
661 *Earth Sciences*, **105**, 797-818.
- 662  
663 Armandita, C., Morley, C.K. & Rowell, P. 2015. Origin, structural geometry, and development of a giant  
664 coherent slide: The South Makassar Strait mass transport complex. *Geosphere*, **11**, 376-403,  
665 <http://doi.org/10.1130/ges01077.1>.
- 666  
667 Brackenridge, R., Nicholson, U., Sapiie, B., Stow, D. & Tappin, D. 2020. Indonesian Throughflow as a  
668 preconditioning mechanism for submarine landslides in the Makassar Strait. *Geological Society,*  
669 *London, Special Publications*, **500**.
- 670  
671 Bull, S. & Cartwright, J.A. 2019. Line length balancing to evaluate multi-phase submarine landslide  
672 development: an example from the Storegga Slide, Norway. *Geological Society, London, Special*  
673 *Publications*, **500**.
- 674

675 Bull, S., Cartwright, J. & Huuse, M. 2009a. A subsurface evacuation model for submarine slope failure.  
676 *Basin Research*, **21**, 433-443, <http://doi.org/10.1111/j.1365-2117.2008.00390.x>.

677

678 Bull, S., Cartwright, J. & Huuse, M. 2009b. A review of kinematic indicators from mass-transport  
679 complexes using 3D seismic data. *Marine and Petroleum Geology*, **26**, 1132-1151,  
680 <http://doi.org/10.1016/j.marpetgeo.2008.09.011>.

681

682 Burberry, C.M. 2015. Spatial and temporal variation in penetrative strain during compression: Insights  
683 from analog models. *Lithosphere*, **7**, 611-624.

684

685 Butler, R. & McCaffrey, W. 2010. Structural evolution and sediment entrainment in mass-transport  
686 complexes: outcrop studies from Italy. *Journal of the Geological Society*, **167**, 617-631.

687

688 Cardona, S., Wood, L.J., Day-Stirrat, R.J. & Moscardelli, L. 2016. Fabric development and pore-throat  
689 reduction in a mass-transport deposit in the Jubilee Gas Field, Eastern Gulf of Mexico: consequences  
690 for the sealing capacity of MTDs *Submarine Mass Movements and their Consequences*. Springer, 27-  
691 37.

692

693 Cardona, S., Wood, L.J., Dugan, B., Jobe, Z. & Strachan, L.J. 2020. Characterization of the Rapanui mass-  
694 transport deposit and the basal shear zone: Mount Messenger Formation, Taranaki Basin, New  
695 Zealand. *Sedimentology*.

696

697 Cartwright, J.A., Trudgill, B.D. & Mansfield, C.S. 1995. Fault growth by segment linkage: an explanation  
698 for scatter in maximum displacement and trace length data from the Canyonlands Grabens of SE Utah.  
699 *Journal of Structural Geology*, **17**, 1319-1326.

700

701 Chopra, S. & Marfurt, K.J. 2007. *Seismic attributes for prospect identification and reservoir*  
702 *characterization*. Society of Exploration Geophysicists Tulsa, Oklahoma.

703

704 Clare, M., Chaytor, J., Dabson, O., Gamboa, D., Georgiopoulou, A., Eady, H., Hunt, J., Jackson, C., *et al.*  
705 2018. A consistent global approach for the morphometric characterization of subaqueous landslides.  
706 *Geological Society, London, Special Publications*, **477**, SP477. 415.

707

708 Cloke, I., Milsom, J. & Blundell, D. 1999. Implications of gravity data from East Kalimantan and the  
709 Makassar Straits: a solution to the origin of the Makassar Straits? *Journal of Asian Earth Sciences*, **17**,  
710 61-78.

711

712 Crawford, B. 1998. Experimental fault sealing: shear band permeability dependency on cataclastic  
713 fault gouge characteristics. *Geological Society, London, Special Publications*, **127**, 27-47.

714

715 Dahlstrom, C. 1969. Balanced cross sections. *Canadian Journal of Earth Sciences*, **6**, 743-757.

716

717 Dalton, T., Paton, D., Oldfield, S., Needham, D. & Wood, A. 2017. The importance of missing strain in  
718 Deep Water Fold and Thrust Belts. *Marine and Petroleum Geology*, **82**, 163-177.

719  
720 Daly, M., Cooper, M., Wilson, I., Smith, D.t. & Hooper, B. 1991. Cenozoic plate tectonics and basin  
721 evolution in Indonesia. *Marine and Petroleum Geology*, **8**, 2-21.

722  
723 Dott, R. 1963. Dynamics of subaqueous gravity depositional processes. *AAPG Bulletin*, **47**, 104-128.

724  
725 Eckersley, A.J., Lowell, J. & Szafian, P. 2018. High-definition frequency decomposition. *Geophysical*  
726 *Prospecting*, **66**, 1138-1143.

727  
728 Ellis, M.A. & Dunlap, W.J. 1988. Displacement variation along thrust faults: Implications for the  
729 development of large faults. *Journal of Structural Geology*, **10**, 183-192.

730  
731 Farrell, S.G. 1984. A dislocation model applied to slump structures, Ainsa Basin, South Central  
732 Pyrenees. *Journal of Structural Geology*, **6**, 727-736.

733  
734 Fossen, H. 2016. *Structural geology*. Cambridge University Press.

735  
736 Frey-Martinez, J., Cartwright, J. & Hall, B. 2005. 3D seismic interpretation of slump complexes:  
737 examples from the continental margin of Israel. *Basin Research*, **17**, 83-108,  
738 <http://doi.org/10.1111/j.1365-2117.2005.00255.x>.

739  
740 Frey-Martínez, J., Cartwright, J. & James, D. 2006. Frontally confined versus frontally emergent  
741 submarine landslides: A 3D seismic characterisation. *Marine and Petroleum Geology*, **23**, 585-604,  
742 <http://doi.org/10.1016/j.marpetgeo.2006.04.002>.

743  
744 Gamboa, D. & Alves, T.M. 2015. Three-dimensional fault meshes and multi-layer shear in mass-  
745 transport blocks: Implications for fluid flow on continental margins. *Tectonophysics*, **647**, 21-32.

746  
747 Gamboa, D., Alves, T. & Cartwright, J. 2011. Distribution and characterization of failed (mega) blocks  
748 along salt ridges, southeast Brazil: Implications for vertical fluid flow on continental margins. *Journal*  
749 *of Geophysical Research: Solid Earth*, **116**.

750  
751 Gee, M., Gawthorpe, R. & Friedmann, J. 2005. Giant striations at the base of a submarine landslide.  
752 *Marine Geology*, **214**, 287-294.

753  
754 Gee, M.J., Masson, D.G., Watts, A.B. & Mitchell, N.C. 2001. Passage of debris flows and turbidity  
755 currents through a topographic constriction: seafloor erosion and deflection of flow pathways.  
756 *Sedimentology*, **48**, 1389-1409.

757  
758 Guntoro, A. 1999. The formation of the Makassar Strait and the separation between SE Kalimantan  
759 and SW Sulawesi. *Journal of Asian Earth Sciences*, **17**, 79-98.

760  
761 Higgins, S., Clarke, B., Davies, R.J. & Cartwright, J. 2009. Internal geometry and growth history of a  
762 thrust-related anticline in a deep water fold belt. *Journal of Structural Geology*, **31**, 1597-1611.

763  
764 Hodgson, D., Brooks, H., Ortiz-Karpf, A., Spychala, Y., Lee, D. & Jackson, C.-L. 2018. Entrainment and  
765 abrasion of megaclasts during submarine landsliding and their impact on flow behaviour. *Geological*  
766 *Society, London, Special Publications*, **477**, SP477. 426.

767  
768 Huiqi, L., McClay, K. & Powell, D. 1992. Physical models of thrust wedges *Thrust tectonics*. Springer,  
769 71-81.

770  
771 Huvenne, V.A., Croker, P.F. & Henriot, J.P. 2002. A refreshing 3D view of an ancient sediment collapse  
772 and slope failure. *Terra Nova*, **14**, 33-40.

773  
774 Jackson, C.A. 2011. Three-dimensional seismic analysis of megaclast deformation within a mass  
775 transport deposit; implications for debris flow kinematics. *Geology*, **39**, 203-206.

776  
777 Jenner, K.A., Piper, D.J., Campbell, D.C. & Mosher, D.C. 2007. Lithofacies and origin of late Quaternary  
778 mass transport deposits in submarine canyons, central Scotian Slope, Canada. *Sedimentology*, **54**, 19-  
779 38.

780  
781 Joanne, C., Lamarche, G. & Collot, J.Y. 2013. Dynamics of giant mass transport in deep submarine  
782 environments: the Matakaoa Debris Flow, New Zealand. *Basin Research*, **25**, 471-488.

783  
784 Koyi, H. 1995. Mode of internal deformation in sand wedges. *Journal of Structural Geology*, **17**, 293-  
785 300.

786  
787 Koyi, H.A., Sans, M., Teixell, A., Cotton, J. & Zeyen, H. 2004. The significance of penetrative strain in  
788 the restoration of shortened layers—Insights from sand models and the Spanish Pyrenees.

789  
790 Lastras, G., Canals, M., Urgeles, R., Hughes-Clarke, J.E. & Acosta, J. 2004. Shallow slides and pockmark  
791 swarms in the Eivissa Channel, western Mediterranean Sea. *Sedimentology*, **51**, 837-850.

792  
793 Liu, S. & Dixon, J.M. 1995. Localization of duplex thrust-ramps by buckling: analog and numerical  
794 modelling. *Journal of Structural Geology*, **17**, 875-886.

795  
796 Mandl, G. & Crans, W. 1981. Gravitational gliding in deltas. *Geological Society, London, Special*  
797 *Publications*, **9**, 41-54.

798  
799 Martinsen, O. & Bakken, B. 1990. Extensional and compressional zones in slumps and slides in the  
800 Namurian of County Clare, Ireland. *Journal of the Geological Society*, **147**, 153-164.

801  
802 Masson, D., Huggett, Q. & Brunnsden, D. 1993. The surface texture of the Saharan debris flow deposit  
803 and some speculations on submarine debris flow processes. *Sedimentology*, **40**, 583-598.

804  
805 Mayer, B. & Damm, P. 2012. The Makassar Strait throughflow and its jet. *Journal of Geophysical*  
806 *Research: Oceans*, **117**.

807  
808 Moernaut, J. & De Batist, M. 2011. Frontal emplacement and mobility of sublacustrine landslides:  
809 results from morphometric and seismostratigraphic analysis. *Marine Geology*, **285**, 29-45.

810  
811 Moore, G.F., Saffer, D., Studer, M. & Pisani, P.C. 2011. Structural restoration of thrusts at the toe of  
812 the Nankai Trough accretionary prism off Shikoku Island, Japan: Implications for dewatering processes.  
813 *Geochemistry, Geophysics, Geosystems*, **12**.

814  
815 Moscardelli, L. & Wood, L. 2008. New classification system for mass transport complexes in offshore  
816 Trinidad. *Basin Research*, **20**, 73-98, <http://doi.org/10.1111/j.1365-2117.2007.00340.x>.

817  
818 Nardin, T.R., Hein, F., Gorsline, D.S. & Edwards, B. 1979. A review of mass movement processes  
819 sediment and acoustic characteristics, and contrasts in slope and base-of-slope systems versus  
820 canyon-fan-basin floor systems.

821  
822 Nemec, W. 1991. Aspects of sediment movement on steep delta slopes. In: Colella, A. & Prior, D.B.  
823 (eds) *Coarsed-Grained Deltas*. International Association of Sedimentologists, **10**, 29-73.

824  
825 Ogata, K., Mountjoy, J., Pini, G.A., Festa, A. & Tinterri, R. 2014a. Shear zone liquefaction in mass  
826 transport deposit emplacement: a multi-scale integration of seismic reflection and outcrop data.  
827 *Marine Geology*, **356**, 50-64.

828  
829 Ogata, K., Pogačnik, Ž., Pini, G.A., Tunis, G., Festa, A., Camerlenghi, A. & Rebesco, M. 2014b. The  
830 carbonate mass transport deposits of the Paleogene Friuli Basin (Italy/Slovenia): internal anatomy and  
831 inferred genetic processes. *Marine Geology*, **356**, 88-110.

832  
833 Omeru, T. 2014. *Mass Transport Deposits: Implications for Reservoir Seals*. Doctor of Philosophy,  
834 Cardiff University.

835  
836 Omeru, T. & Cartwright, J.A. 2019. The efficacy of kinematic indicators in a complexly deformed Mass  
837 Transport Deposit: Insights from the deepwater Taranaki Basin, New Zealand. *Marine and Petroleum*  
838 *Geology*, **106**, 74-87.

839  
840 Omosanya, K.O. & Alves, T.M. 2013. A 3-dimensional seismic method to assess the provenance of  
841 Mass-Transport Deposits (MTDs) on salt-rich continental slopes (Espírito Santo Basin, SE Brazil).  
842 *Marine and Petroleum Geology*, **44**, 223-239.

843  
844 Ortiz-Karpp, A., Hodgson, D.M., Jackson, C.A.-L. & McCaffrey, W.D. 2017. Influence of Seabed  
845 Morphology and Substrate Composition On Mass-Transport Flow Processes and Pathways: Insights  
846 From the Magdalena Fan, Offshore Colombia. *Journal of Sedimentary Research*, **87**, 189-209.

847  
848 Partyka, G., Gridley, J. & Lopez, J. 1999. Interpretational applications of spectral decomposition in  
849 reservoir characterization. *The Leading Edge*, **18**, 353-360.

850



851 Piper, D.J.W., Pirmez, C., Manley, P.L., Long, D., Flood, R.D., Normark, W.R. & Showers, W. 1997. Mass  
852 Transport Deposits of the Amazon Fan. *In: Flood, R.D., Piper, D.J.W., Klaus, A. & Peterson, L.C. (eds.)*  
853 *Ocean Drilling Program, Scientific Results*, 109-146.

854

855 Posamentier, H.W. & Kolla, V. 2003. Seismic geomorphology and stratigraphy of depositional elements  
856 in deep-water settings. *Journal of Sedimentary Research*, **73**, 367-388.

857

858 Posamentier, H.W. & Martinsen, O.J. 2011. The character and genesis of submarine mass-transport  
859 deposits: insights from outcrop and 3D seismic data. *Mass-transport deposits in deepwater settings:*  
860 *Society for Sedimentary Geology (SEPM) Special Publication 96*, 7-38.

861

862 Puspita, S.D., Hall, R. & Elders, C.F. 2005. Structural styles of the offshore West Sulawesi fold belt,  
863 North Makassar Straits, Indonesia. *Thirtieth IPA Annual Convention & Exhibition*. Indonesian  
864 Petroleum Association (IPA), Jakarta.

865

866 Sanderson, D.J. & Marchini, W. 1984. Transpression. *Journal of Structural Geology*, **6**, 449-458.

867

868 Sawyer, D.E., Flemings, P.B., Shipp, R.C. & Winker, C.D. 2007. Seismic geomorphology, lithology, and  
869 evolution of the late Pleistocene Mars-Ursa turbidite region, Mississippi Canyon area, northern Gulf  
870 of Mexico. *AAPG Bulletin*, **91**, 215-234.

871

872 Schnellmann, M., Anselmetti, F.S., Giardini, D. & McKENZIE, J.A. 2005. Mass movement-induced fold-  
873 and-thrust belt structures in unconsolidated sediments in Lake Lucerne (Switzerland). *Sedimentology*,  
874 **52**, 271-289.

875

876 Shanmugam, G. 2012. Origin and Classification of Sandy Mass-Transport Deposits *Handbook of*  
877 *Petroleum Exploration and Production*. Elsevier, **9**, 41-65.

878

879 Shanmugam, G. 2015. The landslide problem. *Journal of Palaeogeography*, **4**, 109-166.

880

881 Sobiesiak, M.S., Kneller, B., Alsop, G.I. & Milana, J.P. 2016. Internal deformation and kinematic  
882 indicators within a tripartite mass transport deposit, NW Argentina. *Sedimentary Geology*,  
883 <http://doi.org/10.1016/j.sedgeo.2016.04.006>.

884

885 Sobiesiak, M.S., Kneller, B., Alsop, G.I. & Milana, J.P. 2018. Styles of basal interaction beneath mass  
886 transport deposits. *Marine and Petroleum Geology*, **98**, 629-639.

887

888 Sobiesiak, M.S., Buso, V.V., Kneller, B., Alsop, G.I. & Milana, J.P. 2019. Block Generation, Deformation,  
889 and Interaction of Mass-Transport Deposits With the Seafloor: An Outcrop-Based Study of the  
890 Carboniferous Paganzo Basin (Cerro Bola, NW Argentina). *Submarine Landslides: Subaqueous Mass*  
891 *Transport Deposits from Outcrops to Seismic Profiles*, 91-104.

892

893 Steventon, M.J., Jackson, C.A., Hodgson, D.M. & Johnson, H.D. 2019. Strain analysis of a seismically  
894 imaged mass-transport complex, offshore Uruguay. *Basin Research*, **31**, 600-620.

895  
896 Strachan, L.J. 2002. *Geometry to genesis: a comparative field study of slump deposits and their modes*  
897 *of formation*. University of Wales. Cardiff.

898  
899 Takagi, H., Pratama, M.B., Kurobe, S., Esteban, M., Aránguiz, R. & Ke, B. 2019. Analysis of generation  
900 and arrival time of landslide tsunami to Palu City due to the 2018 Sulawesi earthquake. *Landslides*, **16**,  
901 983-991.

902  
903 Tappin, D., Watts, P., McMurtry, G., Lafoy, Y. & Matsumoto, T. 2001. The Sissano, Papua New Guinea  
904 tsunami of July 1998—offshore evidence on the source mechanism. *Marine Geology*, **175**, 1-23.

905  
906 Totake, Y., Butler, R.W., Bond, C.E. & Aziz, A. 2018. Analyzing structural variations along strike in a  
907 deep-water thrust belt. *Journal of Structural Geology*, **108**, 213-229.

908  
909 Trincardi, F. & Argnani, A. 1990. Gela submarine slide: a major basin-wide event in the Plio-Quaternary  
910 foredeep of Sicily. *Geo-Marine Letters*, **10**, 13.

911  
912 Van Der Merwe, W.C., Hodgson, D.M. & Flint, S.S. 2011. Origin and terminal architecture of a  
913 submarine slide: a case study from the Permian Vischkuil Formation, Karoo Basin, South Africa.  
914 *Sedimentology*, **58**, 2012-2038, <http://doi.org/10.1111/j.1365-3091.2011.01249.x>.

915  
916 Vanneste, M., Forsberg, C.F., Glimsdal, S., Harbitz, C.B., Issler, D., Kvalstad, T.J., Løvholt, F. & Nadim, F.  
917 2013. Submarine landslides and their consequences: what do we know, what can we do? *Landslide*  
918 *science and practice*. Springer, 5-17.

919  
920 Walsh, J.J. & Watterson, J. 1991. Geometric and kinematic coherence and scale effects in normal fault  
921 systems. *Geological Society, London, Special Publications*, **56**, 193-203.

922  
923 Watt, S., Talling, P., Vardy, M., Masson, D., Henstock, T., Hühnerbach, V., Minshull, T., Urlaub, M., *et*  
924 *al.* 2012. Widespread and progressive seafloor-sediment failure following volcanic debris avalanche  
925 emplacement: Landslide dynamics and timing offshore Montserrat, Lesser Antilles. *Marine Geology*,  
926 **323**, 69-94.

927  
928 Weimer, P. & Shipp, C. 2004. Mass Transport Complexes: Musing on past uses and suggestions for  
929 future directions. *Offshore Technology Conference*, Houston.

930  
931 Zeng, H., Henry, S.C. & Riola, J.P. 1998. Stratal slicing, Part II: Real 3-D seismic data. *Geophysics*, **63**,  
932 514-522.

933 **FIGURE CAPTIONS**

934 **Fig. 1.** Geological setting and location map of the study area. **(a)** The Makassar Strait is surrounded by  
935 tectonically active regions, where Eurasia, Indo-Australia, Philippine Sea and Pacific plates interact. A  
936 strong ocean current flowing from Pacific towards Indian oceans, Indonesia Throughflow (ITF), flows  
937 through the Makassar Strait (red arrow). **(b)** The study area is located in the southern end of Labani  
938 Channel, a narrow strait between Paternoster Platform and western Sulawesi margin. The channel  
939 connects the North and South Makassar basins. Major structural features adjacent to the study area  
940 are fault zones (Palu-Koro and Paternoster fault zones) and fold-thrust belts (e.g. Brackenridge et al.,  
941 2020; Cloke et al., 1999). The fold-thrust belts are divided into the Northern (NSP), Central (CSP) and  
942 Southern (SSP) structural provinces (Puspita et al., 2005). The dark blue line marks the extent of 3D  
943 seismic reflection data, and the green line outlines the area covered by multibeam data. Two green  
944 dots represent wells within the seismic reflection data. The small, yellow area marks the extent of the  
945 Haya Slide (see Fig. 2). Blue and red dots are the location of near-seabed sediment cores of TGS009  
946 and TGS194, respectively. **(c)** A conceptual cross-section across the Makassar Strait showing MTCs  
947 accumulation in the basin and their related sources, i.e. accretionary shelf (related to Mahakam Delta)  
948 in the West and collapse of anticline flanks in the East. Inferred based on Puspita et al. (2005) and  
949 Brackenridge et al. (2020). **(d)** A seismic line correlating the Haya Slide (yellow-shaded) and the two  
950 wells (i.e. XS-1 and XR-1). The sedimentary package containing the slide is Quaternary in age and  
951 predominantly consists of deep-marine (upper-middle bathyal) claystone.

952 **Fig. 2.** Seabed topography, as defined by this bathymetry map, shows the external geometry of the  
953 Haya Slide. The slide originated from the NE (collapse of the southern flank of a thrust-cored anticline)  
954 and transported towards the SW. This study focuses on the toe domain of the slide (red outline), which  
955 is mostly imaged by the 3D seismic reflection data (blue outline). The toe domain of the slide has a  
956 radial geometry, where the Eastern and Northern lateral margins trending N-S and E-W, respectively.

957 **Fig. 3. (a)** Thickness map covering the toe domain of the Haya Slide. The slide is thickest (200 m) in the  
958 southern part and thins toward the Northern Lateral Margin. Laterally, three areas can be defined  
959 based on its frontal geometry (i.e. Area A, B, and C). An inset map showing the focus area of the slide,  
960 captured by 3D seismic reflection data. **(b)** Spectral decomposition map showing internal seismic  
961 facies of the slide. Axially, the slide can be divided into inner and outer parts with 'soft' boundary  
962 between them. The inner part is dominated by debrite containing megaclasts, and the outer part is  
963 dominated by pop-up blocks.

964 **Fig. 4.** Seismic sections across Area A, B, and C, showing similar general characteristics, where debrite  
965 dominates the inner part, and pop-up blocks dominate the outer part. However, the three areas have

966 different characteristics of frontal margin. **(a)** Area A is characterised by frontal confinement and  
967 coherent pop-up blocks. Translation distance was estimated by calculating shortening amount at H1  
968 and 2, i.e. 8-14% shortening equating to 0.6-1.1 km. **(b)** Area B is characterised by frontal ramps with  
969 more chaotic reflections adjacent to frontal margin, and less coherent pop-up blocks. **(c)** Area C is  
970 characterised by frontal emergence and a broad bulge on the seabed above steeply-inclined  
971 detachment surface.

972 **Fig. 5.** Deformation ahead of the parent flow. **(a)** Variance time-slice showing distributed shear zone  
973 downdip from an intact block. Thrusts forming this distributed shear zone laterally propagate  
974 eastwards. **(b)** Seismic section showing distributed shear zone, showing deformed strata ahead  
975 immediately downdip from the intact block. Folded strata ahead of the BSS, interpreted as an  
976 unformed thrust.

977 **Fig. 6.** **(a)** Basal shear surface structure map showing slope gradient break in Area C. **(b)** Seabed  
978 structure map showing a broad area of high seabed relief (seabed bulge). **(c)** Spatial relationship  
979 between slope gradient break on the BSS and the occurrence of the seabed bulge, leading to frontal  
980 emergence of the slide. **(d)** Seismic section adjacent to Northern Lateral Margin showing closely-  
981 spaced pop-up blocks and frontal confinement of the slide.

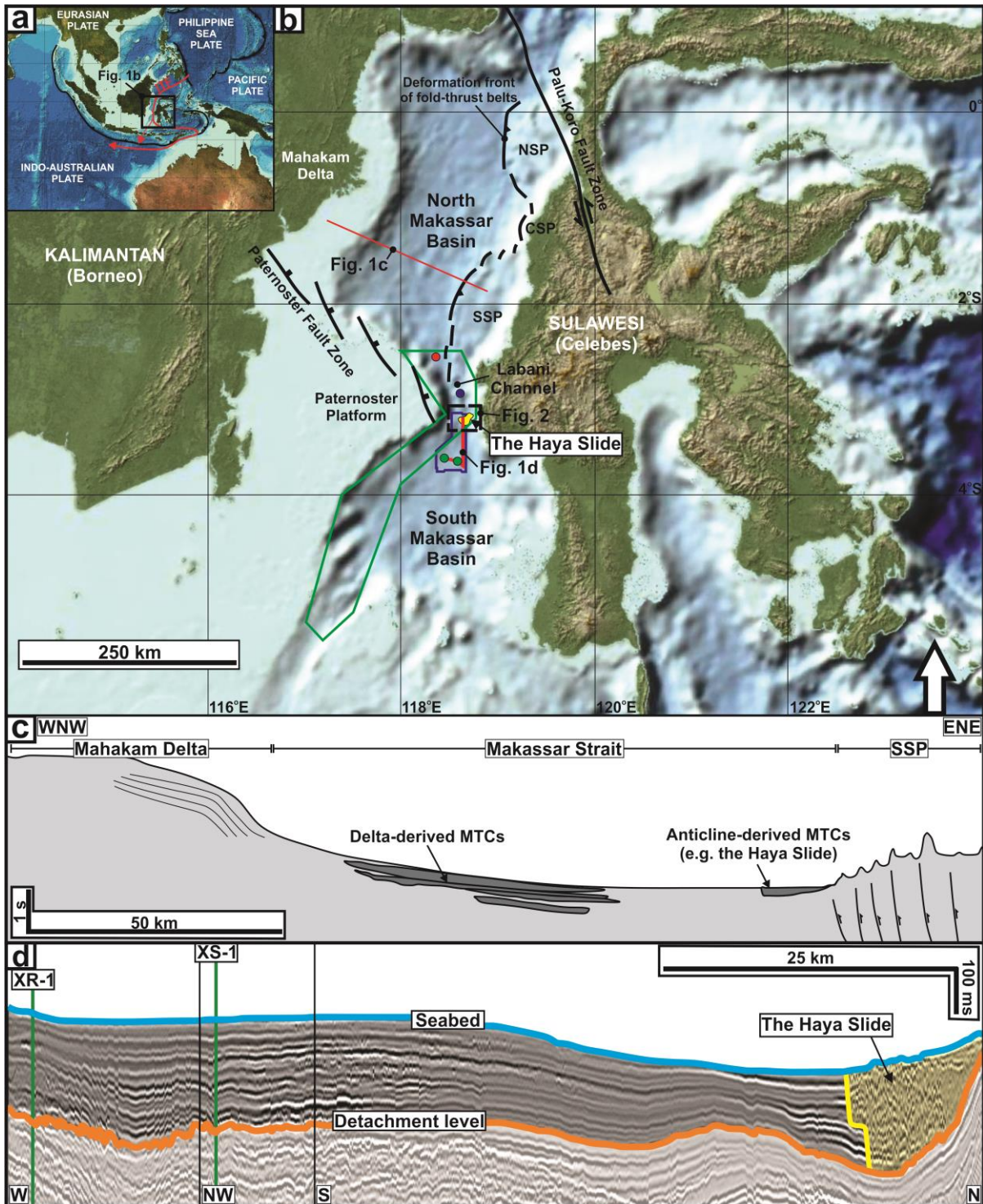
982 **Fig. 7.** **(a)** Variance along the BSS (50 ms windowed above) showing an abrupt boundary between Area  
983 B and C. **(b)** A ramp marks the boundary between Area B and C, and expressed as positive relief on  
984 the seabed.

985 **Fig. 8.** Along-strike quantitative analysis of Pop-up Block 3 (see Fig. 4a). **(a)** Time structure map of H2  
986 (see Fig. 4a) and associated faults. **(b)** Variance time-slice showing lateral extent of Pop-up Block 3. **(c)**  
987 Throw vs. Distance (T-x) plot of fore- and backthrusts bounding Pop-up Block 3. Shear zone separates  
988 two bodies that have different amount of strain, i.e. the area to the west of the shear zone  
989 experienced more contraction as shown by cumulative throw as compared the area eastwards from  
990 the shear zone. **(d-f)** Seismic sections showing along-strike variability of faults bounding Pop-up Block  
991 3.

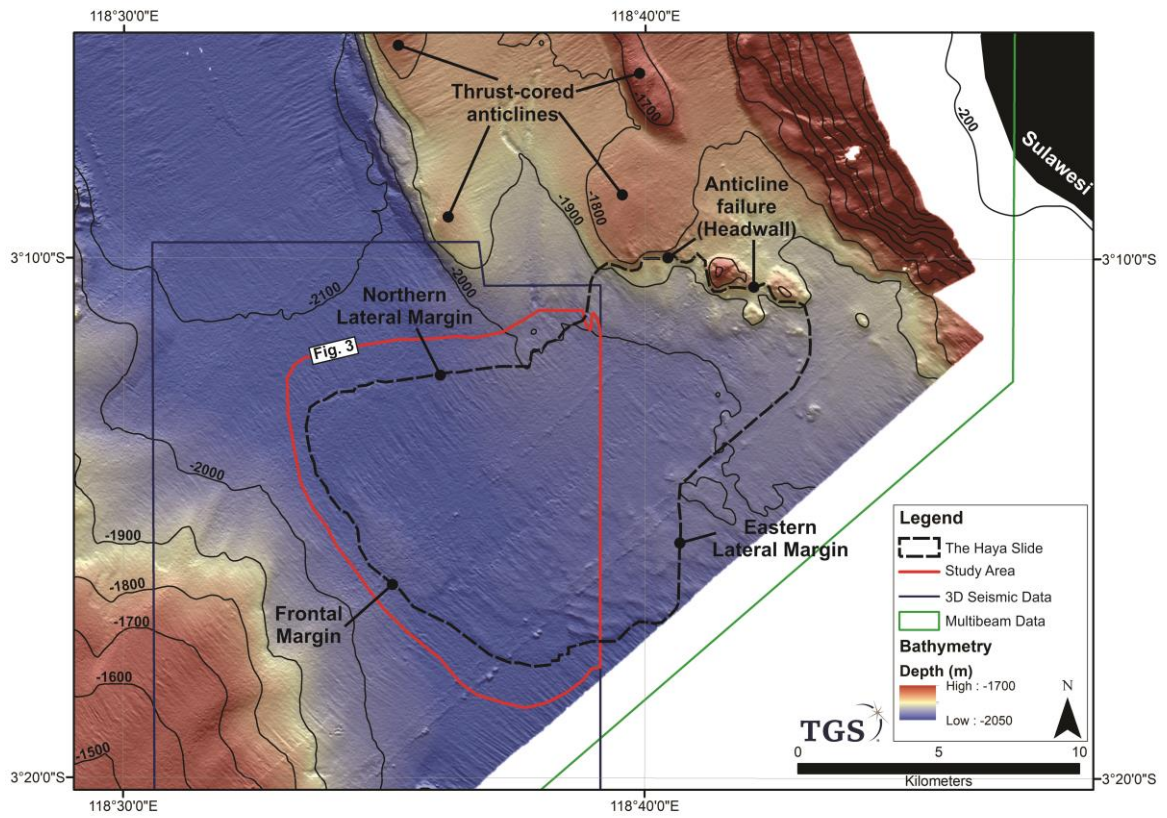
992 **Fig. 9.** Schematic model of emplacement processes of the Haya Slide. **(a)** Debris flow, originated from  
993 failed anticline (see Fig. 2) entered the basin, deformed the seabed, and then entrained substrate into  
994 the flow. **(b)** Substrate erosion and entrainment continued to occur up to the point where the debris  
995 flow did not have sufficient shear stress for substrate entrainment. Thus, the remaining exerted stress  
996 deformed substrate ahead of the flow (i.e. lateral loading). **(c)** Subsequent compressional deformation  
997 occurred, allowing a relatively short translation distance (0.61 to 1.06 km) in the toe domain, which  
998 has different frontal geometries along strike.

999 **Fig. 10.** A summary of downdip and along-strike variations in Areas A, B and C of the Haya Slide., Note  
1000 the lateral changes in structural style and internal facies characteristics.

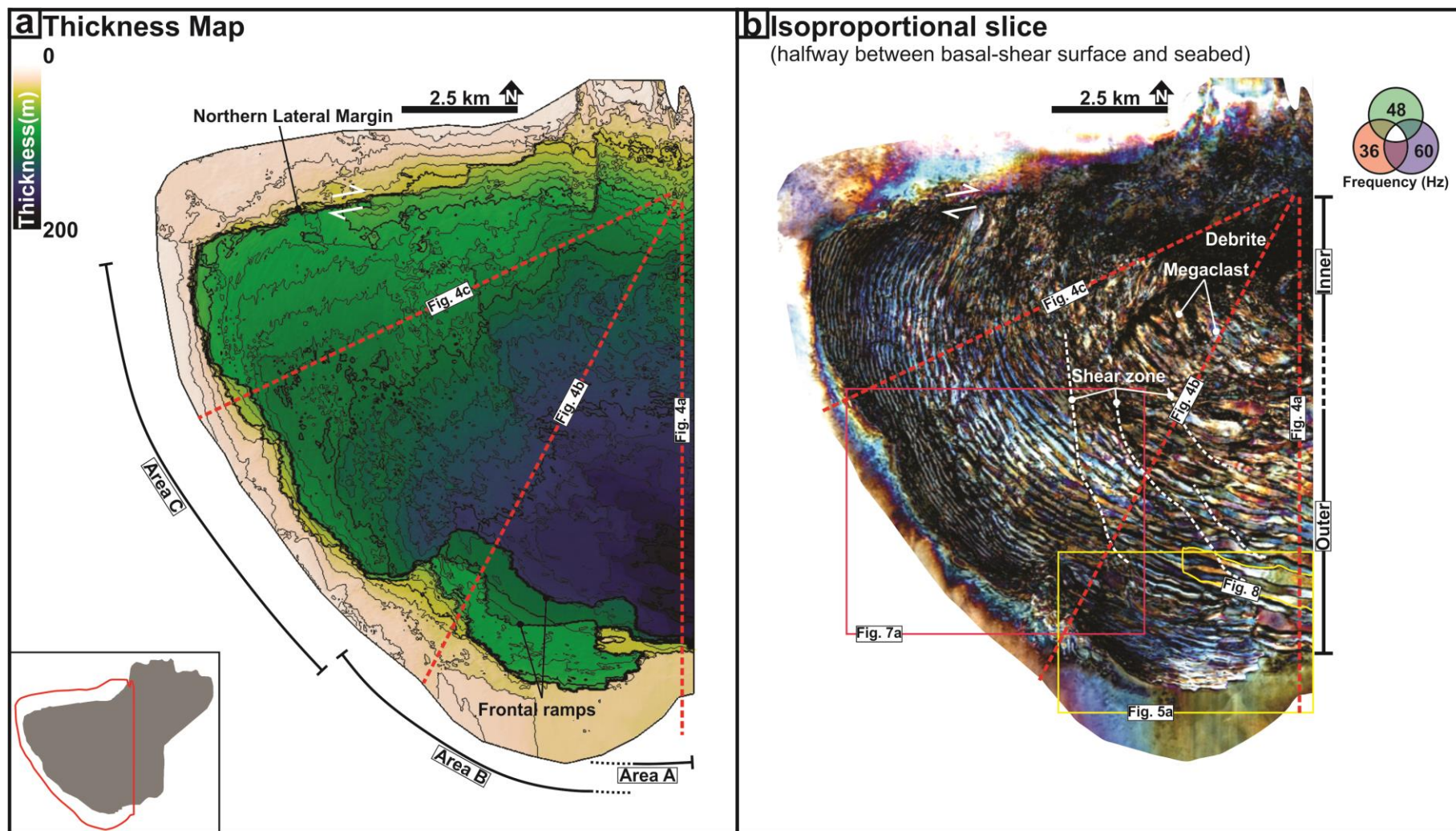
1001 **Fig. 11.** Evolution of basal shear surface adjacent to the toewall of the Haya Slide, showing  
1002 development of **(a)** frontal confinement in Area A, **(b)** frontal emergence in Area C, and **(c)** staircase-  
1003 like frontal ramps in Area B, which is an intermediate (transitional) style between frontal confinement  
1004 and emergence.



1007 Figure 2

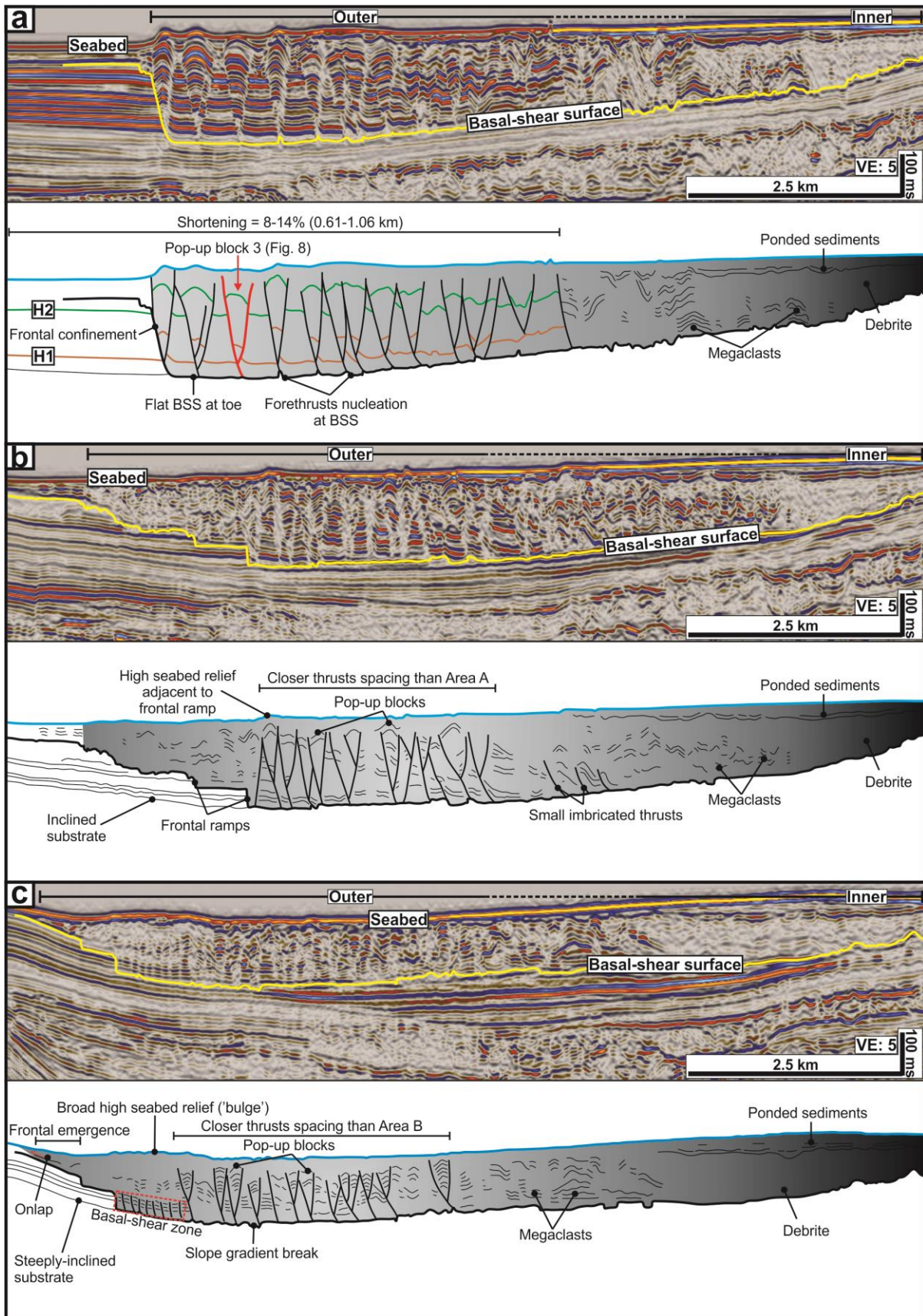


1008

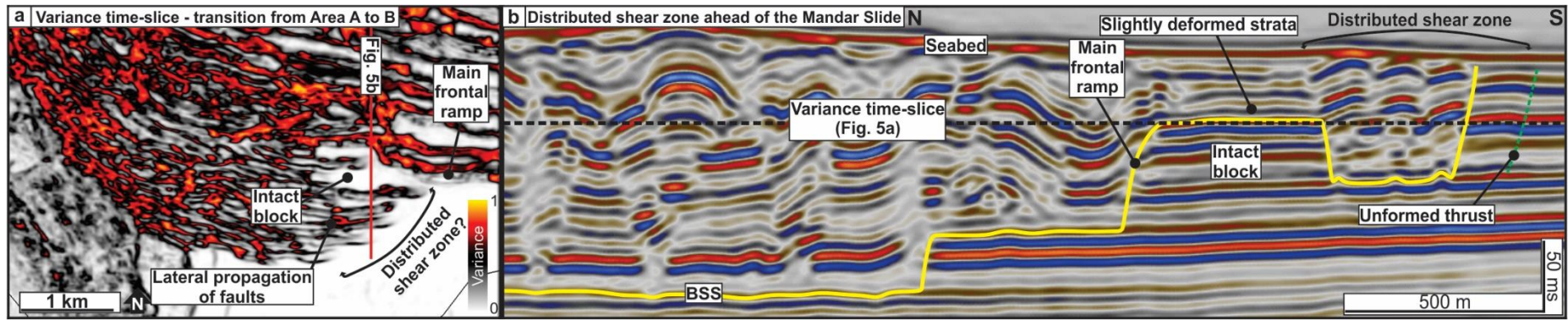




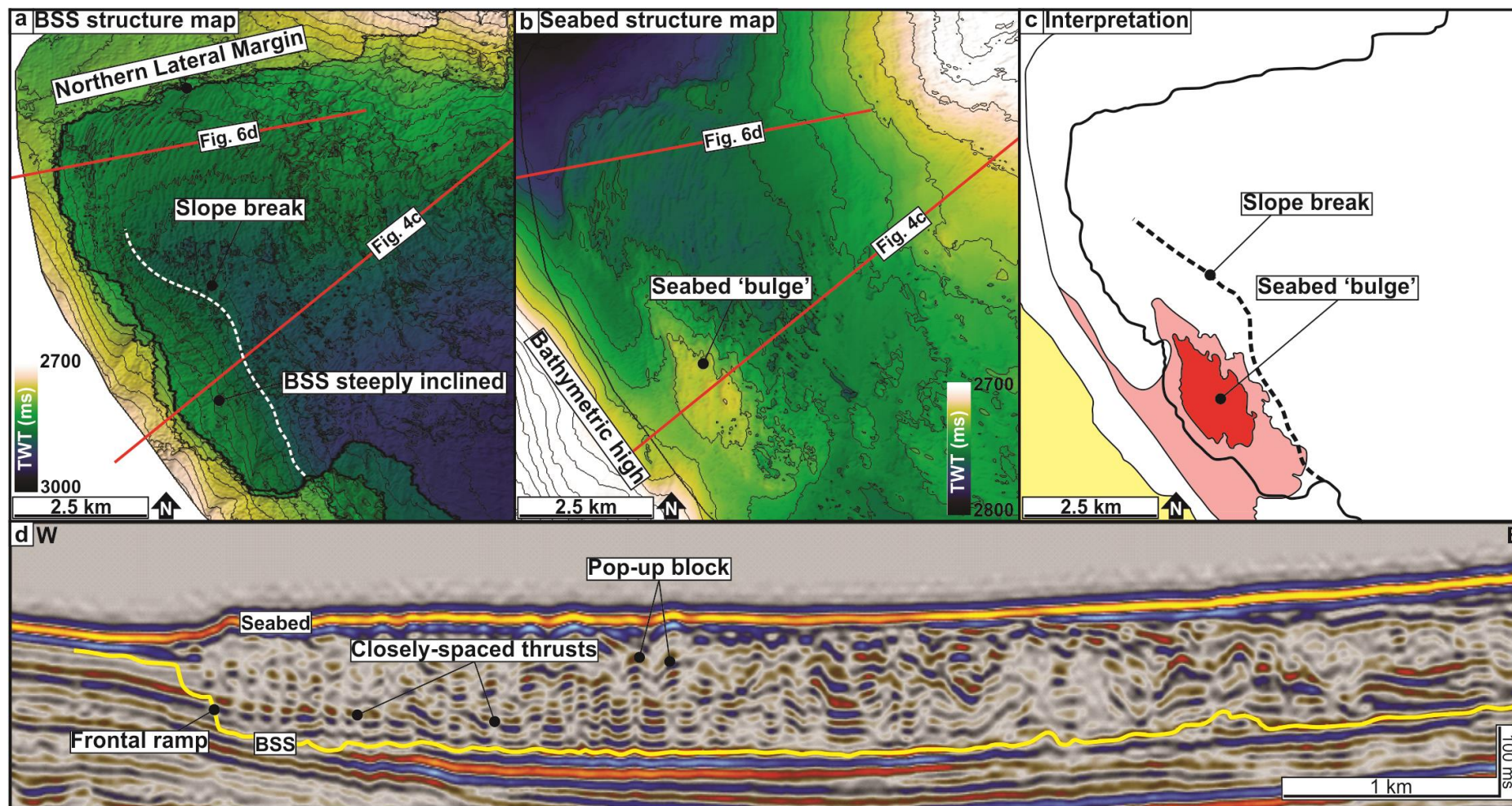
1011 Figure 4



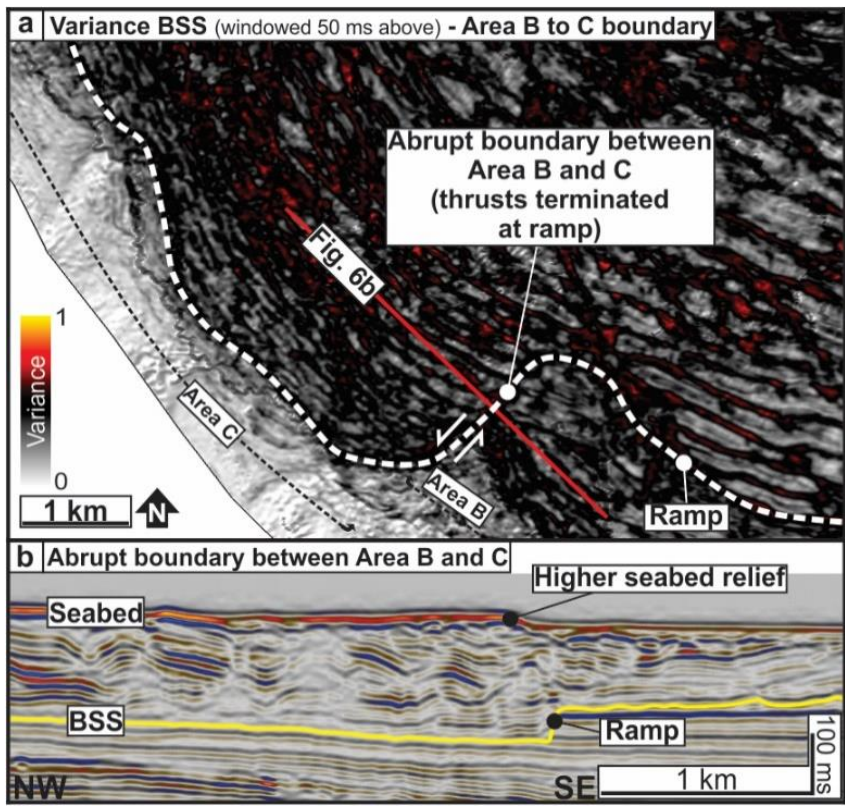
1013 Figure 5



1014



1017 Figure 7



1018

